

# *Spatial radiative feedbacks from internal variability using multiple regression*

Article

Accepted Version

Bloch-Johnson, J. ORCID: <https://orcid.org/0000-0002-8465-5383>, Rugenstein, M. and Abbot, D. S. (2020) Spatial radiative feedbacks from internal variability using multiple regression. *Journal of Climate*, 33 (10). pp. 4121-4140. ISSN 1520-0442 doi: 10.1175/JCLI-D-19-0396.1 Available at <https://centaur.reading.ac.uk/90824/>

It is advisable to refer to the publisher's version if you intend to cite from the work. See [Guidance on citing](#).

To link to this article DOI: <http://dx.doi.org/10.1175/JCLI-D-19-0396.1>

Publisher: American Meteorological Society

All outputs in CentAUR are protected by Intellectual Property Rights law, including copyright law. Copyright and IPR is retained by the creators or other copyright holders. Terms and conditions for use of this material are defined in the [End User Agreement](#).

[www.reading.ac.uk/centaur](http://www.reading.ac.uk/centaur)



1      **Spatial radiative feedbacks from internal variability using multiple**  
2      **regression**

3      Jonah Bloch-Johnson\*

4      *NCAS-Climate, University of Reading, Reading, UK*

5      Maria Rugenstein

6      *Max Planck Institute for Meteorology, Hamburg, Germany*

7      Dorian S. Abbot

8      *Department of the Geophysical Sciences, University of Chicago, Chicago, Illinois, USA*

9      \*Corresponding author address:

10     E-mail: [j.bloch-johnson@reading.ac.uk](mailto:j.bloch-johnson@reading.ac.uk)

## ABSTRACT

11 The sensitivity of the climate to CO<sub>2</sub> forcing depends on spatially-varying  
12 radiative feedbacks which act both locally and nonlocally. We assess whether  
13 a method employing multiple regression can be used to estimate local and  
14 nonlocal radiative feedbacks from internal variability. We test this method on  
15 millennial-length simulations performed with six coupled atmosphere-ocean  
16 general circulation models (AOGCMs). Given the spatial pattern of warming,  
17 the method does quite well at recreating the top-of-atmosphere flux response  
18 for most regions of the Earth, except over the Southern Ocean where it consis-  
19 tently overestimates the change, leading to an overestimate of the sensitivity.  
20 For five of the six models, the method finds that local feedbacks are posi-  
21 tive due to cloud processes, balanced by negative nonlocal shortwave cloud  
22 feedbacks associated with regions of tropical convection. For four of these  
23 models, the magnitude of both are comparable to the Planck feedback, so that  
24 changes in the ratio between them could lead to large changes in climate sen-  
25 sitivity. The positive local feedback explains why observational studies that  
26 estimate spatial feedbacks using only local regressions predict an unstable cli-  
27 mate. The method implies that sensitivity in these AOGCMs increases over  
28 time due to a reduction in the share of warming occurring in tropical convect-  
29 ing regions and the resulting weakening of associated shortwave cloud and  
30 longwave clear-sky feedbacks. Our results provide a step towards an observa-  
31 tional estimate of time-varying climate sensitivity by demonstrating that many  
32 aspects of spatial feedbacks appear to be the same between internal variability  
33 and the forced response.

<sup>34</sup> **1. Introduction**

<sup>35</sup> Forecasting global warming is one of climate science's key challenges. As the atmospheric car-  
<sup>36</sup> bon dioxide concentration increases, the planet's radiation of energy to space becomes less than its  
<sup>37</sup> absorption of sunlight (Arrhenius 1896). This energy imbalance, the *radiative forcing*, warms the  
<sup>38</sup> surface, setting off processes (*radiative feedbacks*) that close the imbalance, restoring the system  
<sup>39</sup> to a new steady state. We call the global average of the radiative feedbacks the *climate feedback*  
<sup>40</sup> (also called the climate feedback parameter, Charney et al. (1979), or the thermal damping rate,  
<sup>41</sup> Dessler (2012)). The total warming in response to a given increase in CO<sub>2</sub> is thus determined by  
<sup>42</sup> the resulting radiative forcing and the climate feedback (Charney et al. 1979). The rate of warming  
<sup>43</sup> also involves the thermal inertia of the surface, mostly due to oceanic heat uptake (Gregory et al.  
<sup>44</sup> 2002). Uncertainty in the climate feedback contributes the most to uncertainty in future warming  
<sup>45</sup> (Otto et al. 2013; Lewis and Curry 2015; Lutsko and Popp 2019), in part because of the inverse  
<sup>46</sup> relationship between feedback and sensitivity (Roe and Baker 2007).

<sup>47</sup> Directly simulating radiative feedbacks is difficult primarily because cloud feedbacks depend  
<sup>48</sup> on small-scale processes (Wetherald and Manabe 1988). Alternatively, the climate feedback can  
<sup>49</sup> be inferred from observations, either by solving for it using the observed warming, observed deep  
<sup>50</sup> ocean heat uptake, and simulated radiative forcing (Gregory et al. 2002; Otto et al. 2013), or by  
<sup>51</sup> analyzing how the planet's energy imbalance changes as the surface temperatures varies month-  
<sup>52</sup> to-month or year-to-year (Forster and Gregory 2006; Murphy et al. 2009; Dessler 2010; Cox et al.  
<sup>53</sup> 2018; Lutsko and Takahashi 2018; Jiménez-de-la Cuesta and Mauritsen 2019; Libardoni et al.  
<sup>54</sup> 2019). These observational methods often assume that the climate feedback is constant, but many  
<sup>55</sup> studies have shown that it typically changes with time in simulations (e.g., Murphy 1995; Wat-  
<sup>56</sup> terson 2000; Senior and Mitchell 2000; Armour et al. 2012; Jonko et al. 2012; Andrews et al.

57 2015). While the temperature dependence of feedbacks can cause this to occur under sufficient  
58 (and likely strong) warming (Meraner et al. 2013; Bloch-Johnson et al. 2015), the change occurs  
59 even after relatively small amounts of warming (e.g., Armour et al. 2012; Andrews et al. 2015;  
60 Rugenstein et al. 2016). Since warming in different regions sets off radiative feedbacks of differ-  
61 ent strengths, the inconstancy of the climate feedback is likely caused by the change in the spatial  
62 pattern of warming with time (Winton et al. 2010; Armour et al. 2012). Since the temperature  
63 pattern associated with internal variability differs from the forced response, we should expect the  
64 climate feedback associated with each to differ (Dessler 2012; Colman and Hanson 2017), and in  
65 fact the climate feedback appears to vary across the historical record (Gregory and Andrews 2016;  
66 Fueglistaler 2019). The climate feedback may vary between historical and future warming (Zhou  
67 et al. 2016; Armour 2017; Proistosescu and Huybers 2017; Andrews et al. 2018), although the  
68 importance of this effect may be modest (Lewis and Curry 2018).

69 Recent modelling work has explored a new framework in which the climate feedback is a linear  
70 combination of radiative feedbacks associated with different regions of the surface, weighted by  
71 the temperature change in each region (Zhou et al. 2017; Dong et al. 2019). This assumes that  
72 the spatial radiative feedbacks themselves are constant, with only the map of surface tempera-  
73 ture change evolving. This paper explores a corollary: since internal variability creates an ever-  
74 changing pattern of surface temperature and top-of-atmosphere radiative imbalance, a sufficiently  
75 long record of this variability should exhibit the behavior of these spatial radiative feedbacks. In  
76 this paper, we propose and evaluate a multiple regression (MR) method to estimate the spatial  
77 radiative feedbacks of six atmosphere-ocean general circulation models from control simulations,  
78 which we compare to existing methods for estimating feedbacks from internal variability (Section  
79 2). We do so in spite of the known bias in regression methods related to stochastic variation in  
80 top-of-atmosphere fluxes (Spencer and Braswell 2008, 2011; Choi et al. 2014; Proistosescu et al.

81 2018). We test the method by convolving the estimated spatial feedbacks with warming patterns  
 82 from forced simulations performed with the respective models (Section 3), assessing the method's  
 83 accuracy in recreating aspects of the forced response. We discuss insights the MR method pro-  
 84 vides into climate dynamics, such as the competing nature of local and nonlocal cloud feedbacks  
 85 (Section 4) and summarize our findings (Section 5).

## 86 2. Illustrating the MR method with a conceptual model

87 In this section, we present a method for predicting spatial feedbacks from records of unforced  
 88 variability using multiple regression. We first set up a conceptual climate model designed to illus-  
 89 trate the method and capture some features of the complex climate models discussed in Section 3.  
 90 This conceptual model has two regions of equal area. In each, the change in surface temperature  
 91 ( $T_i$ ) is proportional to the net energy gain of that region, which is the sum of the net downwards  
 92 top-of-atmosphere (TOA) radiative flux ( $N_i$ ), the net gain from horizontal energy transport from  
 93 the atmosphere and ocean combined ( $-H$  in region 1,  $H$  in region 2), and additional random  
 94 forcing ( $F_{surf,i}$ ):

$$c_1 \frac{dT_1}{dt} = N_1 - H + F_{surf,1} \quad (1)$$

$$c_2 \frac{dT_2}{dt} = N_2 + H + F_{surf,2} \quad (2)$$

95 where  $c_i$  is the surface thermal inertia associated with region  $i$ . This model can be re-expressed in  
 96 terms of anomalies relative to an initial equilibrium state, so that we consider  $T'_i$ ,  $N'_i$ ,  $H'$ , and  $F'_{surf,i}$   
 97 instead of  $T_i$ ,  $N_i$ ,  $H$ , and  $F_{surf,i}$ . We assume that heat transport is proportional to the temperature  
 98 gradient between the two regions:

$$H' = \gamma(T'_1 - T'_2) \quad (3)$$

99 Changes in a region's top-of-atmosphere radiative fluxes are caused by radiative feedbacks ( $\lambda_{i,j}$ ,  
100 which represents the influence of surface temperature in region  $j$  on the net TOA flux in region  $i$ ),  
101 radiative forcing due to changes in a forcing agent such as an increase in CO<sub>2</sub> ( $F_{CO_2,i}$ ), and radiative  
102 forcing due to random atmospheric fluctuations that occur independently of surface temperature  
103 ( $F_{TOA,i}$ ):

$$N'_1 = \lambda_{1,1}T'_1 + \lambda_{1,2}T'_2 + F_{CO_2,1} + F_{TOA,1} \quad (4)$$

$$N'_2 = \lambda_{2,1}T'_1 + \lambda_{2,2}T'_2 + F_{CO_2,2} + F_{TOA,2} \quad (5)$$

104  $\lambda_{1,1}$  and  $\lambda_{2,2}$  are local radiative feedbacks, while  $\lambda_{1,2}$  and  $\lambda_{2,1}$  are nonlocal radiative feedbacks  
105 (where our sign convention ensures that a negative  $\lambda$  implies a negative, stabilizing feedback).

106 Nonlocal radiative feedbacks (Rugenstein et al. 2016; Zhou et al. 2017; Po-Chedley et al. 2018;  
107 Dong et al. 2019) are changes in a region's top-of-atmosphere flux that occur due to changes in  
108 surface temperature elsewhere, independent of local surface temperature changes. For example, in  
109 Figure 1, regions 1 and 2 represent the convecting and subsiding branches of an overturning cell  
110 respectively. Surface warming in region 1 propagates vertically, warming region 1's free tropo-  
111 sphere, and then horizontally into the free troposphere of region 2, increasing  $H'$ . Region 2 now  
112 has a warmer troposphere, which radiates more, decreasing  $N'_2$ . The resulting horizontal advection  
113 may also increase the humidity of region 2's free troposphere, increasing  $N'_2$ . Assuming region 2  
114 has a subsidence-induced boundary layer inversion, its low cloud cover could also increase, caus-  
115 ing a further decrease in  $N'_2$ . All of these changes in  $N'_2$  occur independently of any changes in  $T'_2$ ,  
116 and conspire to make  $\lambda_{2,1}$  positive or negative.

117 We note that an increase in  $H'$  will also increase  $T'_2$  directly (Eq. 1; Feldl and Roe 2013b). While  
118 this latter effect is connected to nonlocal radiative feedbacks in that both occur due to horizontal  
119 fluxes of heat and moisture, the two effects are different, and can disagree in the sign of the

120 resulting surface warming, as demonstrated by the above example. While the influence of  $H'$  on  
 121 surface temperature is important for understanding the evolution of the spatial pattern of warming,  
 122 in this paper we are focused only on the influence of surface temperature on TOA radiative fluxes,  
 123 and so we focus on nonlocal radiative feedbacks.

124 Suppose that region 1 has a weak positive local feedback  $\lambda_{1,1} = 0.5 \text{ Wm}^{-2}\text{K}^{-1}$  (red solid line,  
 125 Figure 2b), and a stronger negative nonlocal feedback, so that  $\lambda_{2,1} = -2 \text{ Wm}^{-2}\text{K}^{-1}$  (light blue  
 126 solid line, Figure 2b). We also assume that the surface temperature of the subsiding region 2 has  
 127 no net effect on TOA fluxes, so that  $\lambda_{1,2} = \lambda_{2,2} = 0 \text{ Wm}^{-2}\text{K}^{-1}$  (orange and gray solid lines in  
 128 Figure 2b). We assume that region 2's thermal inertia is much larger than region 1's, representing  
 129 more ocean heat uptake in this region (see Appendix for details).

130 We define the global climate feedback  $\lambda$  to be the dependence of the globally averaged net TOA  
 131 flux on the globally averaged surface temperature, that is

$$\lambda(t) = \frac{\partial \bar{N}}{\partial \bar{T}}(t) = \sum \left( \Lambda \frac{d\vec{T}}{dt}(t) \right) / \frac{d\bar{T}}{dt}(t) \quad (6)$$

132 where  $\vec{T} = \begin{bmatrix} T_1 \\ T_2 \end{bmatrix}$ ,  $\Lambda = \begin{bmatrix} \lambda_{1,1} & \lambda_{2,1} \\ \lambda_{1,2} & \lambda_{2,2} \end{bmatrix}$ , and a bar over a vector indicates the global average of that vector.  
 133 We do not have to use an anomaly for  $\bar{N}$  because  $\bar{N}$  is 0 in equilibrium. Note that even though  
 134 the spatial feedbacks  $\Lambda$  are constant, the global feedback  $\lambda$  can change with time because of the  
 135 evolving spatial pattern of warming  $\frac{d\vec{T}}{dt}(t)$ .

136 We perform two 5000-year experiments: a “control” experiment, where all variations in  
 137  $\vec{T}'_{control}(t)$  and  $\vec{N}'_{control}(t)$  are due to random forcing at the surface ( $\vec{F}'_{surf}(t) = \begin{bmatrix} F'_{surf,1}(t) \\ F'_{surf,2}(t) \end{bmatrix}$ ) and TOA  
 138 ( $\vec{F}_{TOA}(t) = \begin{bmatrix} F'_{TOA,1}(t) \\ F'_{TOA,2}(t) \end{bmatrix}$ ), and an “abrupt4x” experiment in which the time series  $\vec{T}'_{abrupt4x}(t)$  and  
 139  $\vec{N}'_{abrupt4x}(t)$  also respond to an initial step forcing akin to a quadrupling of CO<sub>2</sub> concentration  
 140 ( $F_{CO_2,1} = F_{CO_2,2} = 8 \text{ Wm}^{-2}$ ).

141 For the abrupt4x simulation, the climate feedback  $\lambda = \frac{\partial \bar{N}}{\partial \bar{T}'}$  changes significantly around year  
 142 20. We therefore define two forced feedbacks,  $\lambda_{4x,early}$  and  $\lambda_{4x,later}$ , which are the slopes of the  
 143 linear regressions of  $\bar{N}_{abrupt4x}(t)$  against  $\bar{T}'_{abrupt4x}(t)$  taken over years 1 to 20 and years 21 to 5000  
 144 respectively (Figure 2c). Before these regressions are taken, we average each annual time series  
 145 (gray dots) over roughly exponentially increasing time periods (colored dots).  $\Delta\lambda_{4x} \equiv \lambda_{4x,later} -$   
 146  $\lambda_{4x,early}$  is the change in feedback between the periods.

147 We seek a method to predict  $\lambda_{4x,early}$ ,  $\lambda_{4x,later}$ , and  $\Delta\lambda_{4x}$  given  $\vec{T}'_{control}(t)$  and  $\vec{N}'_{control}(t)$  (internal  
 148 variability), and  $\vec{T}'_{abrupt4x}(t)$  (the spatial pattern of warming). The simplest method would be to  
 149 regress annual averages of  $\bar{N}_{control}(t)$  against  $\bar{T}_{control}(t)$  to get the resulting regression slope  $\lambda_{control}$   
 150 (the slope of the blue line in Figure 2a), and to assume that  $\lambda_{4x,early} = \lambda_{4x,later} = \lambda_{control}$  (Forster  
 151 and Gregory 2006; Murphy et al. 2009; Dessler 2010). We call this the “global” method because  
 152 it uses information about changes in global surface temperature only.

153 The radiative feedbacks associated with temperature change induced by random forcing (i.e.,  
 154  $\vec{F}_{surf}$  and  $\vec{F}_{TOA}$ ) differ from those induced by uniform greenhouse forcing ( $\vec{F}_{CO_2}$ ) (Dessler 2012;  
 155 Colman and Hanson 2017; Proistosescu et al. 2018). Our conceptual model illustrates how this can  
 156 arise from spatial variation. Since the thermal inertia in region 2 is larger, most of the temperature  
 157 variability occurs in region 1, so that  $\lambda_{control}$  is weighted towards the feedbacks associated with  
 158 this region ( $\lambda_{control} \approx \lambda_{1,1} + \lambda_{2,1}$ ). The spatial pattern of warming in the forced response is initially  
 159 dominated by region 1 as well, once more because it has the lowest thermal inertia. As a result, the  
 160 global method predicts  $\lambda_{4x,early}$  well (see Figure 2c and d). However, the global method always  
 161 predicts  $\Delta\lambda_{4x} = 0$ , as it assumes a constant  $\lambda$ . Since warming moves to region 2 over time and  
 162  $\lambda_{1,2} + \lambda_{2,2} > \lambda_{1,1} + \lambda_{2,1}$ ,  $\Delta\lambda_{4x}$  is positive. As a result, the global method underpredicts the warming  
 163 of the abrupt4x simulation by about 1.5 K (Figure 2c). To address this shortcoming, we need a  
 164 method that accounts for the spatial variation of feedbacks.

165 The “local” method is a commonly used method (Boer and Yu (2003b), Crook et al. (2011), the  
 166 “local” method in Feldl and Roe (2013a), Brown et al. (2015), and Trenberth et al. (2015)) for  
 167 estimating spatial feedbacks. In this method, we construct  $\vec{\lambda}_{local} = \begin{bmatrix} \lambda_{1,local} \\ \lambda_{2,local} \end{bmatrix}$  where  $\lambda_{i,local}$  is the  
 168 result of regressing  $N'_{i,control}(t)$  against  $T'_{i,control}(t)$ . Taking the dot product of  $\vec{\lambda}_{local}$  with  $\vec{T}'_{abrupt4x}(t)$   
 169 then provides an estimate of  $\vec{N}'_{abrupt4x}(t)$  which we can use to estimate  $\lambda_{4x,early}$ ,  $\lambda_{4x,late}$ , and  $\Delta\lambda_{4x}$ .  
 170 This method assumes all radiative feedbacks are local, while allowing for the nonlocal effects of  
 171 heat transport (Feldl and Roe 2013b). However, if there are nonlocal radiative feedbacks, then the  
 172 local method can miss or conflate their effects. In region 1, estimates of  $\lambda_{1,local}$  tend toward  $\lambda_{1,1} =$   
 173  $0.5 \text{ Wm}^{-2}\text{K}^{-1}$  (dotted red line, Figure 2b), missing the negative nonlocal feedback  $\lambda_{2,1}$ . Since  
 174 the early period is dominated by warming in region 1, the local method overestimates  $\lambda_{4x,early}$   
 175 (where “overestimates” implies the estimate of  $\lambda_{4x,early}$  is more positive than the true value, even  
 176 if both are negative, resulting in an overestimate of the sensitivity). On the other hand,  $T'_2$  tends  
 177 to be positively correlated with  $T'_1$ , due to heat transport, while  $T'_1$  tends to be anti-correlated with  
 178  $N'_2$  because  $\lambda_{2,1}$  is negative. As a result, the local method predicts that  $\lambda_{2,local}$  is negative (dotted  
 179 orange line, Figure 2b), even though  $T'_2$  has no net influence on  $N$ . Since  $T'_2$  contributes more  
 180 to warming over time, the local method incorrectly predicts a more negative feedback (Figure 2c  
 181 and d). Similar discrepancies can occur when local feedbacks are used to diagnose feedbacks  
 182 in GCMs, which may explain instances when the local method fails to predict feedback changes  
 183 properly (Rose et al. 2014). We need a method that includes nonlocal feedbacks while accounting  
 184 for correlation between temperature in different regions.

185 We propose a multiple regression (“MR”) method, which estimates the local and nonlocal feed-  
 186 backs associated with  $N'_i$  (that is, the influence of  $T'_1$  and  $T'_2$  on  $N'_i$ ) by regressing  $N'_{i,control}(t)$  against

187 both regions simultaneously:

$$N'_{i,control}(t) = \lambda_{i,1,MR} T'_{1,control}(t) + \lambda_{i,2,MR} T'_{2,control}(t) + F_{TOA,i} \quad (7)$$

188 In least squares multiple regression,  $\lambda_{i,j,MR}$  is the same as the slope of the regression of  $N'_{i,control}(t)^*$   
189 against  $T'_{j,control}(t)^*$ , where the star indicates that each time series is the residual after regressing  
190 against the surface temperatures in all non- $j$  regions (see Appendix). This removes the effect of  
191 correlations between surface temperature in different regions giving spurious feedbacks, as with  
192  $\lambda_{2,local}$  above. Multiple regression has been used to estimate other surface temperature-dependent  
193 feedbacks from internal variability, though not radiative feedbacks (Liu et al. 2008; Li et al. 2012;  
194 Li and Forest 2014; Liu et al. 2018). The dashed lines in Figure 2b show that, given sufficient  
195 time, the MR method predicts the local and nonlocal feedbacks in each region, so that when we  
196 multiply the full matrix of estimated spatial feedbacks  $\Lambda_{MR} = \begin{bmatrix} \lambda_{1,1,MR} & \lambda_{1,2,MR} \\ \lambda_{2,1,MR} & \lambda_{2,2,MR} \end{bmatrix}$  by  $\vec{T}'_{abrupt,4x}(t)$  to  
197 estimate  $\vec{N}_{abrupt4x}(t)$ , the resulting estimates  $\lambda_{4x,early}$ ,  $\lambda_{4x,late}$ , and  $\Delta\lambda_{4x}$  are accurate (Figure 2c  
198 and d). Therefore, for this example, the MR method is able to account for the difference in climate  
199 feedback between internal variability and the forced response.

200 Random fluctuations in  $N$  influence  $T$  via planetary energy gain at the same time that  $T$  influ-  
201 ences  $N$  via radiative feedbacks. As a result,  $T$  will tend to lag  $N$  with a positive correlation, while  
202  $N$  will lag  $T$  with a negative correlation, so that regressions taken without a lag will be biased to-  
203 wards 0 (Spencer and Braswell 2008, 2011; Choi et al. 2014; Proistosescu et al. 2018). This issue  
204 does not occur for random forcing at the surface, which only affects  $N$  indirectly through radiative  
205 feedbacks. Therefore, the more stochastic forcing that occurs at TOA ( $\vec{F}_{TOA}$ ) as opposed to the  
206 surface ( $\vec{F}_{surf}$ ), the more the regression of  $N$  vs.  $T$  will overestimate the true radiative feedback.  
207 For the example in Figure 2,  $F_{surf,1}$  and  $F_{surf,2}$  are white noise with variance  $20 \text{ W}^2\text{m}^{-4}$ , while  
208  $F_{TOA,1}$  and  $F_{TOA,2}$  are white noise with variance  $5 \text{ W}^2\text{m}^{-4}$ . Figure S1 shows a case where these

209 variances are 10 and 15  $\text{W}^2\text{m}^{-4}$  respectively, with the result that all three regression methods over-  
210 estimate  $\lambda_{4x,early}$  and  $\lambda_{4x,later}$ , while underestimating  $\Delta\lambda_{4x}$ . In other words, given sufficient random  
211 TOA forcing, regression estimates of spatial feedbacks will be biased. We consider this bias in  
212 discussing our results in the next section.

213 It should be mentioned that Proistosescu et al. (2018) model ENSO variability as a distinct  
214 additional mechanism by which  $N$  and  $T$  mutually influence each other, which similarly leads  
215 to overestimates of  $\lambda$  from regression-based methods. As part of their model, they assume that  
216  $T$  influences  $N$  with a lag of about three months. Since this is beyond the time scale of most  
217 atmospheric processes, we assume that this feedback propagates in part through the ocean, so that  
218 the atmospheric component may still operate through the same spatial feedbacks that operate under  
219 other forms of variability and under the forced response (e.g., it could occur due to a “tropical  
220 atmospheric bridge” mechanism; Klein et al. 1999).

### 221 3. Using the MR method on AOGCMs

222 To test the methods discussed above on atmosphere-ocean general circulation models  
223 (AOGCMs), we use simulations from LongRunMIP, an archive of fully coupled millennial-length  
224 simulations of complex climate models (Rugenstein et al. 2019). We chose the six models with  
225 millennial-length control and abrupt4x simulations for which we have monthly output. Details of  
226 these models and simulations are given in Table S1.

227 We alter the three methods from Section 2 to reflect the more complex nature of AOGCMs:

- 228
  - $\text{CO}_2$  forcing can lead to atmospheric changes that are independent of surface warming. These  
229 “adjustments” to forcing occur mostly within the first year (e.g., Gregory and Webb 2008).

230 We remove this year from our analysis, redefining our early period to be years 2 to 20.

- 231 • For AOGCMs, there are more than two regions with distinct behaviors. Dividing our models  
 232 into  $n$  regions, equation 7 becomes

$$N'_i(t) = \lambda_{i,1,MR} T'_{1,control}(t) + \lambda_{i,2,MR} T'_{2,control}(t) + \dots + \lambda_{i,n,MR} T'_{n,control}(t) + F_{TOA,i}, \quad (8)$$

233 giving a system of  $n$  equations

$$\vec{N}'(t) = \Lambda \vec{T}'(t) + \vec{F}_{TOA} \quad (9)$$

234 where  $\Lambda$  is a matrix of feedbacks  $\lambda_{i,j}$ . Each equation in this system has  $n - 1$  degrees of  
 235 freedom, so  $n$  must be smaller than the length of the control simulation, and preferably much  
 236 smaller given the significant spatial correlation of surface temperature. For simplicity, we  
 237 divide the surface equally in latitude and longitude, although this may miss features of the  
 238 climate system. Since our control simulations last at least 1000 years (Table S1), we use a  
 239  $15^\circ$  by  $15^\circ$  grid, giving 288 regions (Figure 3).

- 240 • Circulations, and therefore radiative feedbacks, change with season. Thus, we compute feed-  
 241 backs for each season individually, first by averaging all monthly time series into seasonal  
 242 time series (where the seasons are DJF, MAM, JJA, SON), and then performing a separate re-  
 243 gression for each season (e.g. all DJF values of  $\vec{N}'_{control}(t)$  against all DJF values of  $\vec{T}'_{control}(t)$ )  
 244 creating a set of four feedbacks. We multiply each month of  $\vec{T}'_{4x}(t)$  by the relevant seasonal  
 245 feedback, and take the annual average to estimate  $\vec{N}'_{4x}(t)$ . We compare seasonal averages to  
 246 other approaches in Tables S2 and S3. While seasonal averaging tends to reduce the error in  
 247 the MR method, the qualitative behavior of the different methods is not affected by the choice  
 248 of time averaging.

249 Figures 3 and 4 show  $\bar{N}$  vs.  $\bar{T}'$  of the control and abrupt4x simulations of the six models respec-  
 250 tively. Figure 4 also shows  $\bar{N}$  estimated using the three methods, assuming that each estimate starts

251 with the true value of  $\bar{N}$  at year 2. The solid lines in Figure 4 are local regressions of  $\bar{N}$  against  $\bar{T}'$   
252 performed using LOESS (LOcally Estimated Scatterplot Smoothing; Cleveland and Devlin 1988,  
253 see Appendix for more detail). We can use the slopes of these lines mapped against the time series  
254 of  $\bar{T}$  to estimate feedbacks as a function of time (lines in Figure 5).

255 Though there is a range of feedback values between models, all six forced simulations have a  
256 feedback that gets less negative with time (black lines), consistent with past results for similar  
257 models (Andrews et al. 2015). The MR method (green lines) matches or overestimates the feed-  
258 back value, with this error tending to decrease with time. This error can range from  $\sim 1 \text{ Wm}^{-2}\text{K}^{-1}$   
259 for the early years of CESM104 and GISSE2R (that is, at least half of the feedback strength itself)  
260 to roughly 0 for HadCM3L. The MR method correctly predicts that the feedback gets less negative  
261 with time, although for some of the models it underestimates the magnitude of the change.

262 The global method (blue) overestimates the early feedback. Since the global method is agnostic  
263 about the pattern of surface warming, the predicted feedback is mostly constant except for small  
264 differences due to changes in the seasonal distribution of warming and in seasonal feedbacks (e.g.,  
265 the early years of HadCM3L). As a result, as the true feedback increases with time, it becomes  
266 more positive than the global estimate for half the models. For some models, this allows the global  
267 method to more accurately forecast the equilibrium warming than the other methods, albeit due to  
268 compensating errors in the early and later periods (i.e., CESM104 and MPIESM12 in Figure 4).

269 The local method (orange) predicts a positive feedback for all models except GISSE2R, implying  
270 a climate unstable to external forcing, and does not predict the increase in feedback with time seen  
271 in all models.

272 The dots in Figure 5 represent estimates of  $\lambda_{4x,early}$  and  $\lambda_{4x,later}$  (feedbacks before and after year  
273 20; see Appendix for details). We visualize the estimates of these feedbacks and their difference  
274 using a scatter plot (black dots in Figure 6), as in Figure 2d. The global and MR methods perform

275 similarly for  $\lambda_{4x,early}$  and  $\lambda_{4x,late}$ , while the MR method gets closer to accurately predicting  $\Delta\lambda_{4x}$ ,  
276 consistent with the discussion around Figure 4 and reflected by the root mean square errors in  
277 Table 1 (for feedback values for all models and components, see Tables S7 and S8).

278  $\vec{N}'$  and  $\lambda$  can be expressed as the sum of shortwave (SW) and longwave (LW) terms, which can  
279 be separated in turn into clear-sky (fluxes recalculated as if no clouds were present) and cloud  
280 terms (the residual of total and clear-sky terms; cloud feedbacks defined this way may include  
281 changes in cloud masking rather than in clouds themselves (Soden et al. 2004)).

282 Examining these component individually shows that the error in  $\lambda_{4x,early}$  in the MR and global  
283 methods is due primarily to SW cloud feedbacks (red markers in Figures 6a and b). Both the  
284 MR and global methods have smaller errors in  $\lambda_{4x,late}$  (Figures 6d and e), but for the MR method  
285 this is caused by a reduction in the error in SW cloud, while for the global method this is due  
286 to offsetting errors in the SW and LW cloud feedbacks (see also Table 1). Cloud feedbacks are  
287 similarly the cause of the local method's large overestimation, while the local method outperforms  
288 the other methods at predicting the primarily local SW clear feedback (Table 1). Note that the  
289 global method has a relatively small error for the LW clear feedback, consistent with Lutsko and  
290 Takahashi (2018). The increase in feedback with time ( $\Delta\lambda_{4x}$ ) and the variation in this increase  
291 between models is driven by the SW cloud feedback (Figures 6g, h, and i). The MR method has  
292 the smallest error in estimating  $\Delta\lambda_{4x}$ , with this error tending to be an underestimate. Figures S2-5  
293 show feedback time series plots for all component fluxes.

294 All methods examined contain some degree of error. We can find the geographic source of these  
295 errors by looking at the true and estimated normalized change in  $\vec{N}'_{4x}$  (multi-model mean in Fig-  
296 ure 7; errors in the multi-model mean and for individual models in Figures S6-S8), calculated by  
297 taking the finite difference in  $\vec{N}'_{4x}(t)$  between the first and last part of the indicated time period,  
298 where each part contains similar amounts of warming (see Appendix). The difference is normal-

299 ized by the global temperature change, allowing intermodel comparison. For the global method,  
300 we make this estimate by regressing  $\vec{N}'_{control}(t)$  against  $\vec{T}'_{control}(t)$  (the “global” method in Feldl and  
301 Roe (2013a) and the “local contribution” in Boer and Yu (2003a,b); Crook et al. (2011); Zelinka  
302 et al. (2012); Andrews et al. (2015)) and using this as the predicted normalized change in  $\vec{N}'_{4x}$ .

303 The MR method does quite well at recreating the multi-model spatial pattern of TOA flux  
304 change, both for net and component fluxes (Figures S9-S12), with the exception of regions south  
305 of 30°S and the north Atlantic. The MR method also overestimates the change in these regions in  
306 individual models (Figures S6-S8). The error in these regions has contributions from all compo-  
307 nent fluxes, foremost the SW cloud feedback (for multi-model mean component flux errors, see  
308 Figures S13-17). For all periods, models, and fluxes except for SW clear-sky (which is primarily  
309 a local feedback), the MR method outperforms the other two methods when scored by the area-  
310 weighted root mean square error (Table 2; for comparison with annual or monthly approaches, see  
311 Table S3; for values for individual models, see Table S4; for details on the error metric, see Ap-  
312 pendix). Specifically, the global method has large compensating errors, especially in the tropics,  
313 and the local method overestimates the change almost everywhere (Figures S6-S8).

314 There are several potential explanations for the MR method’s overestimate for TOA fluxes south  
315 of 30°S and over the north Atlantic. These may be regions where there is significantly more  
316 stochastic forcing at TOA than at the surface, resulting in a similar overestimation to that discussed  
317 in Section 2 and shown in Figure S1. Alternatively, the spatial feedbacks that influence  $\vec{N}'$  in these  
318 regions may be nonlinear, either in that they change in value as the world warms (e.g., a reduction  
319 in the strength of the SW clear feedback once sea ice melts), or the effect of warming in different  
320 regions combines nonlinearly, as might occur in response to circulation changes such as a shift in  
321 the mid-latitude jet; or surface fluxes may influence  $\vec{N}'$  there independently of surface warming.  
322 Further research is needed to diagnose this error.

323 In spite of this overestimate, the MR method can be used to explain the multi-model forced  
324 TOA flux response for roughly three quarters of the Earth using feedbacks estimated from internal  
325 variability (see Table S5 and S6, which show the same error metrics as Tables 1 and 2, using only  
326 TOA fluxes north of 30°S). We now discuss the spatial feedbacks estimated by the MR method, as  
327 well as some of their implications.

## 328 4. Discussion

329 We first test if the spatial feedbacks estimated using the MR method exhibit behavior broadly  
330 consistent with physically modelled feedbacks. The  $i^{th}$  column of  $\Lambda$  represents the change in  $\bar{N}'$   
331 from warming in region  $i$ . Zhou et al. (2017) performed fixed-SST experiments with the CAM5  
332 model where the temperature in region  $i$  was perturbed. The top row of Figure 8 shows spatial  
333 cloud feedbacks for three representative regions calculated using this approach. The bottom row  
334 shows the multi-model and multi-season mean response for warming in similar regions estimated  
335 by the MR method. For both approaches, warming in the extratropics or in regions of tropical  
336 subsidence produces cloud feedbacks that are mostly local and positive, while warming in tropical  
337 convecting regions has significant nonlocal feedbacks which are mostly negative. Since the mod-  
338 els, region sizes, and degree of perturbation differ, the details and magnitudes of the feedbacks  
339 differ. Further, the fixed-SST method allows land temperatures to evolve freely, so that regions  
340 that have significant nonlocal effects, like tropical convecting regions, can cause large changes in  
341 TOA fluxes over land (Figure 8b). The MR method is able to estimate land feedbacks directly, so  
342 that TOA flux changes due to land warming are not included in these tropical convecting feedbacks  
343 (Figure 8e). See also Figure 4 in Dong et al. (2019).

344 The top left panel of Figure 9 shows a map of the multi-model and multi-month mean spatial  
345 feedbacks estimated by the MR method: the change in  $\bar{N}$  caused by warming in each region di-

346 vided by that region's fractional area (so that smaller, polar regions do not have artificially smaller  
347 feedbacks). Spatial feedbacks are strongly negative in regions of tropical convection (e.g., Indone-  
348 sia and Central America) and are mostly positive over the tropical oceans in regions of atmospheric  
349 subsidence as well as much of the extratropical oceans, in keeping with the examples from Fig-  
350 ure 8. These strongly negative feedbacks are robust when feedbacks are recalculated using just  
351 the first or second half of the control simulations (Figures S18-22), although outside these regions  
352 there is some noise, with the sign of roughly a third of net feedback cells differing between the  
353 first and second halves. The variation in the spatial pattern is largely determined by the SW cloud  
354 feedback (bottom left panel, Figure 9; for all flux components, see Figures S19-S22).

355 *a. Local and nonlocal feedbacks*

356 The MR method allows us to split spatial feedbacks into local (the diagonal elements of  $\Lambda$ , giving  
357 the influence of warming on TOA fluxes directly overhead) and nonlocal components (the off-  
358 diagonal elements of  $\Lambda$ ), and to calculate the local and nonlocal components of the map of spatial  
359 feedbacks (middle and right columns of Figure 9 respectively). We note that the devision between  
360 local and nonlocal feedbacks depends on grid resolution, with local feedbacks in coarser grids  
361 incorporating more nonlocal processes. For the grid considered in this paper, the local feedback  
362 is positive almost everywhere, due to cloud feedbacks (Figures S21 and S22): in the tropics and  
363 in subtropical subsiding regions, local warming reduces lower tropospheric stability, leading to  
364 a loss of low clouds and a positive SW cloud feedback (Klein and Hartmann 1993; Wood and  
365 Bretherton 2006; Zhou et al. 2017; Dong et al. 2019). This result holds for each AOGCM except  
366 for GISSE2R, which lacks a positive local SW cloud feedback (Figure S24, Table S8). For most  
367 models, there is a partially compensating negative local LW cloud feedback in tropical convecting  
368 regions, possibly due to an iris effect (Lindzen et al. 2001; Mauritsen and Stevens 2015). Outside

369 of the tropics, there is a positive local LW cloud feedback, possibly associated with an increase in  
370 middle and high cloudiness as convection increases (Zelinka et al. 2012).

371 Positive local feedbacks provide an explanation for observational studies that use the local  
372 method to predict spatial feedbacks, finding that they are positive over much of the Earth and  
373 in the global mean (Brown et al. 2015; Trenberth et al. 2015). For example, the multi-model mean  
374 feedbacks estimated using the local method (top middle panel, Figure S23) resemble the feedbacks  
375 in the upper right panel of Figure 10 from Trenberth et al. (2015). While local method feedbacks  
376 can differ from the local component of MR method feedbacks due to correlation between temper-  
377 ature in different regions as discussed in Section 2, the observational studies provide evidence that  
378 real world local feedbacks are substantially positive. If we use the MR method to estimate the  
379 local components of  $\lambda_{4x,early}$  and  $\lambda_{4x,later}$  (Table S8), we get positive values for all models except  
380 GISS-E2R. For these models, the mean estimated local feedback is  $3.37 \text{ Wm}^{-2}\text{K}^{-1}$  for the early  
381 period and  $3.13 \text{ Wm}^{-2}\text{K}^{-1}$  for the late period (Tables S8).

382 The MR method implies that in the absence of negative nonlocal feedbacks, five out of six of  
383 these AOGCMs would be unstable to radiative forcing, even accounting for the dominant stabiliz-  
384 ing Planck feedback. The MR method predicts that there are strongly negative nonlocal feedbacks  
385 coming from regions of tropical convection (upper right panel, Figure 9), largely due to the SW  
386 cloud feedback (lower right panel). This is consistent with tropical convecting regions behaving  
387 similarly to region 1 of the conceptual model from Section 2: surface warming in the convecting  
388 tropics propagates throughout the tropical free troposphere, increasing the temperature aloft while  
389 leaving surface temperatures alone. This increases the lower tropospheric stability, and thus low  
390 cloud cover (a negative SW cloud feedback), as well as the troposphere's outgoing longwave radi-  
391 ation (a negative LW clear feedback) (Rose and Rayborn 2016; Andrews and Webb 2017; Ceppi  
392 and Gregory 2017; Klein et al. 2017; Zhou et al. 2017; Dong et al. 2019). Note that incorporating

393 these nonlocal interactions changes both local and total values of the LW clear feedback, giving  
394 different values than studies that analyze this feedback purely locally (e.g., Koll and Cronin 2018).

395 For the five models with positive local components, the average nonlocal component of the  
396 abrupt4x feedbacks is  $-4.21 \text{ Wm}^{-2}\text{K}^{-1}$  for the early period and  $-3.69 \text{ Wm}^{-2}\text{K}^{-1}$  for the late  
397 period (Table S8). so that the net forced climate feedback is a small residual between competing  
398 local and nonlocal feedbacks, with local and nonlocal feedbacks strongly anti-correlated between  
399 different models (Table S8; the correlation coefficient for early period non-GISSE2R local vs.  
400 nonlocal feedbacks is  $-0.96$ , and for late is  $-0.98$ ). A modest shift in the relative strength of  
401 these feedbacks (for example, due to a shift in circulation) could lead to large changes in cli-  
402 mate sensitivity; an increase in the local feedback of only a third would be enough to make these  
403 AOGCMs unstable (local and nonlocal feedbacks differ by  $\sim 1 \text{ Wm}^{-2}\text{K}^{-1}$ , which is on average  
404 roughly a third of the magnitude of the local feedback for the non-GISSE2R models). Additional  
405 research is needed to understand what mechanisms cause the anti-correlation between local and  
406 nonlocal feedback strength, and whether we expect this cancellation to hold in different climate  
407 states. Given that the local/nonlocal cancellation does not hold in all contexts – for example, the  
408 nonlocal feedback’s seasonal cycle has a larger amplitude and is more latitudinally constrained  
409 than the local feedback’s seasonal cycle (Figure S25) – it is unlikely that this cancellation is purely  
410 a statistical artifact. Our findings have bearing for exoplanet research, as they suggest that it may  
411 be harder to have a cloudy atmosphere with a stable climate than previously thought (Leconte et al.  
412 2013), potentially reducing the chance of finding habitable worlds.

413 *b. The cause of the increase in climate feedback over time*

414 For all six models, the change in feedback with time ( $\Delta\lambda_{4x}$ ) is positive, primarily because of the  
415 SW cloud feedback, and secondarily the LW clear feedback (Figure 4 and Table S7). The MR

416 method gets the correct sign of  $\Delta\lambda_{4x}$  but underestimates this increase for each model, once more  
417 primarily due to the SW cloud feedback (Table S8).

418 We can estimate how much the change in the spatial pattern of warming with time (Figure 10a)  
419 contributes to  $\Delta\lambda_{4x}$  by multiplying this change by the MR estimate of the spatial pattern of feed-  
420 backs for each flux component (Figure 9, Figures S18-S22). The resulting maps show the contri-  
421 bution of the change in warming pattern to the change in feedback (Figures 10b-f).

422 The MR method identifies two main latitude bands that contribute to the increase in feedback  
423 with time: the tropics, whose convecting regions increase the SW cloud and LW clear feedbacks  
424 (less warming in these regions reduces the role of the strongly negative nonlocal feedbacks dis-  
425 cussed above, consistent with Andrews and Webb 2017; Ceppi and Gregory 2017; Dong et al.  
426 2019; Fueglistaler 2019); and the Southern Ocean, which increases the SW clear feedback (due to  
427 the delayed warming in this region leading to the delayed melting of sea ice). The MR method  
428 estimates that the LW clear sky and SW cloud feedback have offsetting negative contributions in  
429 the Southern Ocean. While the LW clear sky offset is consistent with the total change in the LW  
430 clear feedback being small, and with the LW clear TOA flux change getting more negative in the  
431 Southern Ocean due to a more strongly negative local feedback (zonal figures in the top row of  
432 Figure S19), the change in the SW cloud TOA flux is too negative in this region (lower left panel  
433 of Figure S17), suggesting that the SW cloud negative contribution is an error, and is likely the  
434 reason for the MR method's underestimate of  $\Delta\lambda_{4x}$ .

435 While the exact evolution of temperature patterns in the tropics in AOGCMs may be incorrect  
436 due to cold-tongue biases (Seager et al. 2019), our findings match with Dong et al. (2019), in that  
437 as long as the feedbacks in tropical convecting regions are far more negative than anywhere else,  
438 the delayed warming in regions of ocean heat uptake will ensure an increase in sensitivity over  
439 time. Observational evidence suggests that  $\bar{N}$  depends on tropical midtropospheric temperatures

<sup>440</sup> (Dessler et al. 2018; Ceppi and Gregory 2019; Fueglisterler 2019), supporting our argument that a  
<sup>441</sup> reduction in the share of surface warming occurring in the tropical convecting regions which set  
<sup>442</sup> these temperatures likely influences the Earth's sensitivity.

<sup>443</sup> **5. Conclusions**

<sup>444</sup> The global climate feedback, one of the key parameters in determining future climate change,  
<sup>445</sup> is inconstant in part because radiative feedbacks vary spatially. The MR method estimates these  
<sup>446</sup> spatial feedbacks from records of its internal variability, and improves upon existing methods for  
<sup>447</sup> doing so by incorporating both local and nonlocal radiative responses to surface warming. For  
<sup>448</sup> the six atmosphere-ocean general circulation models studied, the spatial feedbacks estimated by  
<sup>449</sup> the MR method applied to the pattern of surface warming recreate the spatial pattern of top-of-  
<sup>450</sup> atmosphere flux response to forcing more accurately than existing methods, as well as providing  
<sup>451</sup> better estimates of the change in feedback with time. The method consistently overestimates  
<sup>452</sup> the change in TOA flux over the Southern Ocean and north Atlantic, and so overestimates the  
<sup>453</sup> sensitivity. The method finds that that there are significant negative nonlocal feedbacks associated  
<sup>454</sup> with regions of tropical convection, and that the reduction in the share of warming that occurs  
<sup>455</sup> in these regions over time contributes to an increase in the global feedback with time in these  
<sup>456</sup> models, consistent with recent studies (Andrews and Webb 2017; Ceppi and Gregory 2017; Dong  
<sup>457</sup> et al. 2019; Fueglisterler 2019).

<sup>458</sup> The MR method finds that five of the six AOGCMs have strongly positive local cloud feedbacks  
<sup>459</sup> countered by strongly negative nonlocal cloud feedbacks. These positive local feedbacks may  
<sup>460</sup> explain why studies that use local regressions to estimate spatial feedbacks from observed internal  
<sup>461</sup> variability find that they are on average positive (Brown et al. 2015; Trenberth et al. 2015). While  
<sup>462</sup> the AOGCMs exhibit an anti-correlation between local and nonlocal feedbacks, a small relative

463 shift in the balance between these feedbacks could cause large changes in sensitivity, and such  
464 shifts may be relevant for paleoclimate or future warming. Given the large magnitudes associated  
465 with these local and nonlocal cloud feedbacks, it may be harder for cloudy exoplanets to have  
466 stable atmospheres, reducing the chances of finding habitable worlds.

467 Spatial feedbacks estimated from observations could potentially improve warming forecasts and  
468 serve as emerging constraints on AOGCMs. The success of the MR method for most fluxes and  
469 regions of the Earth (with the important exception of Southern Ocean cloud feedbacks) suggests  
470 that many of the spatial feedbacks at work under global warming are observable under internal  
471 variability. Challenges remain to applying the MR method to observations. We would need to  
472 reduce the information necessary to fit our statistical model to be less than the length of the satellite  
473 record; to remove changes in forcing from records of top-of-atmosphere fluxes; and to account for  
474 systematic biases in the observations themselves. We would also need to account for regions of the  
475 Earth and states of the climate where the MR method is biased, such as for Southern Ocean cloud  
476 feedbacks. Furthermore, since spatial feedbacks are just one link in the coupled energy balance  
477 of the climate, we would need complementary theory to complete the forecast of future warming,  
478 particularly its spatial pattern. Still, our results suggest that the processes that will determine the  
479 sensitivity in both the near and far future may be observable today.

480 *Acknowledgments.* This paper was inspired by conversations with Kyle Armour, Cristian Prois-  
481 toescu, Daniel Koll, and Elizabeth Moyer and was improved further by discussions with B. B.  
482 Cael, Yue Dong, Jonathan Gregory, Malte Jansen, Thorsten Mauritsen, Brian Rose, Hansi Singh,  
483 M Wu, and Chen Zhou. The research would not have been possible without the efforts of the  
484 contributors to the LongRunMIP project. The authors thank Chen Zhou for permission to use the  
485 top row in Figure 8. We acknowledge support from the National Science Foundation under NSF

486 award number 1623064. This project has received funding from the European Research Coun-  
487 cil (ERC) under the European Union’s Horizon 2020 research and innovation programme (grant  
488 agreement No 786427, project “Couplet”). Our work was completed with resources provided by  
489 the University of Chicago Research Computing Center, with special thanks to Hossein Pourreza.  
490 We also thank three anonymous reviewers for their insightful comments and our editor, Timothy  
491 Delsole, for his guidance throughout the publication process.

492 **APPENDIX**

493 **Data and methods**

494 *a. Data/code access*

495 For LongRunMIP data access, visit <http://www.longrunmip.org/>. This paper’s code is  
496 available at <https://github.com/jsbj/spatial>.

497 *b. Matrix and vector notation*

498 Note that in the main body of the text, time is treated as continuous, so that time-series are  
499 written as functions (e.g.,  $\vec{T}(t)$  is the evolving spatial pattern of warming). Since the Appendix  
500 documents the calculations we have employed, it treats time as discrete, and so time is instead  
501 treated as an additional dimension (e.g.,  $\mathbf{T}$  is the evolving spatial pattern of warming). Therefore,  
502 a vector in the main body of the text refers to a spatial pattern, while a vector in the Appendix  
503 refers to a time-series of a scalar value (such as a global average).

504 *c. Conceptual model*

505 The conceptual model is a system of stochastic differential equations:

$$\begin{aligned} c_1 \frac{dT'_1}{dt} &= N'_1 - H' + F_{surf,1} \\ c_2 \frac{dT'_2}{dt} &= N'_2 + H' + F_{surf,2} \end{aligned}$$

506 where  $H' = \gamma(T'_1 - T'_2)$  and

$$N'_1 = \lambda_{1,1}T'_1 + \lambda_{1,2}T'_2 + F_{CO_2,1} + F_{TOA,1} \quad (A1)$$

$$N'_2 = \lambda_{2,1}T'_1 + \lambda_{2,2}T'_2 + F_{CO_2,2} + F_{TOA,2} \quad (A2)$$

507 The thermal inertia  $c_i$  is defined as  $m_i \rho c_p$ , where  $\rho$  and  $c_p$  are the density and specific heat of  
 508 ocean water respectively, and  $m_i$  is an equivalent mixed layer depth;  $m_1$  is 50m, and  $m_2$  is 1000m.  
 509  $F_{CO_2,1} = F_{CO_2,2}$  are both  $0 \text{ Wm}^{-2}$  ( $8 \text{ Wm}^{-2}$ ) for the control (abrupt4x) simulation.  $\lambda_{1,1} = 0.5$   
 510  $\text{Wm}^{-2}\text{K}^{-1}$ ,  $\lambda_{2,1} = -2 \text{ Wm}^{-2}\text{K}^{-1}$ ,  $\lambda_{1,2} = \lambda_{2,2} = 0 \text{ Wm}^{-2}\text{K}^{-1}$ , and  $\gamma = 2 \text{ Wm}^{-2}\text{K}^{-1}$ . The terms  
 511  $\vec{F}_{surf}$  and  $\vec{F}_{TOA}$  are white noise processes. In the example shown in Figure 2, the variance of  $F_{surf,1}$   
 512 and  $F_{surf,2}$  is  $40 \text{ Wm}^{-2}$  and the variance of  $F_{TOA,1}$  and  $F_{TOA,2}$  is  $5 \text{ Wm}^{-2}$ , while for the example  
 513 in Figure S1, the variance of  $F_{surf,1}$  and  $F_{surf,2}$  is  $10 \text{ Wm}^{-2}$  and the variance of  $F_{TOA,1}$  and  $F_{TOA,2}$   
 514 is  $15 \text{ Wm}^{-2}$ .

515 *d. The multiple regression method*

516 Suppose that we have a time series of surface temperatures and TOA radiative fluxes of the  
 517 Earth, real or simulated, where the surface of the Earth is regredded into  $n_{grid}$  (288) regions, and  
 518 where we have  $n_{time}$  years of monthly observations. For each season  $s$  ( $1 \leq s \leq 4$ ), we can define an  
 519  $n_{time} \times n_{grid}$  matrix  $\mathbf{T}_m$ , where the element in row  $i$  and column  $j$ ,  $T_{i,j,s}$ , is the surface temperature

520 in region  $j$  during season  $s$  of year  $i$ . We can also define a matrix of anomalies,  $\mathbf{T}'_s$ , where

$$\mathbf{T}'_s = \begin{bmatrix} T_{1,1,s} & T_{1,2,s} & \dots & T_{1,n_{grid},s} \\ T_{2,1,s} & T_{2,2,s} & \dots & T_{2,n_{grid},s} \\ \vdots & \vdots & \ddots & \vdots \\ T_{n_{time},1,s} & T_{n_{time},2,s} & \dots & T_{n_{time},n_{grid},s} \end{bmatrix} - \frac{1}{n_{time}} \begin{bmatrix} \sum_{i=1}^{n_{time}} T_{i,1,s} & \sum_{i=1}^{n_{time}} T_{i,2,s} & \dots & \sum_{i=1}^{n_{time}} T_{i,n_{grid},s} \\ \sum_{i=1}^{n_{time}} T_{i,1,s} & \sum_{i=1}^{n_{time}} T_{i,2,s} & \dots & \sum_{i=1}^{n_{time}} T_{i,n_{grid},s} \\ \vdots & \vdots & \ddots & \vdots \\ \sum_{i=1}^{n_{time}} T_{i,1,s} & \sum_{i=1}^{n_{time}} T_{i,2,s} & \dots & \sum_{i=1}^{n_{time}} T_{i,n_{grid},s} \end{bmatrix}$$

521 To estimate the spatial feedbacks associated with a TOA radiative flux of type  $f$  (where  $f$  is  
 522 either *net*, *LW clear*, *SW clear*, *LW cloud*, or *SW cloud*) and season  $s$ , we first define an  $n_{time} \times$   
 523  $n_{grid}$  matrix of anomalies  $\mathbf{R}'_{f,s}$ , which is analogous to  $\mathbf{T}'_s$  above ( $N$  from the main body of the text  
 524 is  $R_{net}$ ). We can fit the statistical model defined in Equation 9 using least squares to solve for  
 525 seasonal spatial feedbacks ( $\Lambda_{f,s}$ ):

$$\Lambda_{f,s} = \begin{bmatrix} \lambda_{f,1,1} & \lambda_{f,1,2} & \dots & \lambda_{f,1,n_{grid}} \\ \lambda_{f,2,1} & \lambda_{f,2,2} & \dots & \lambda_{f,2,n_{grid}} \\ \vdots & \vdots & \ddots & \vdots \\ \lambda_{f,n_{grid},1} & \lambda_{f,n_{grid},2} & \dots & \lambda_{f,n_{grid},n_{grid}} \end{bmatrix} = (\mathbf{T}'_s^T \mathbf{T}'_s)^{-1} \mathbf{T}'_s^T \mathbf{R}'_{f,s} \quad (A3)$$

526

527 Seasonal feedbacks are used in Section 3, but Section 2 uses an annual version, in which case  
 528 instead of a set of four seasonal feedback matrices, only one feedback matrix estimated using the  
 529 above Equation d, with the difference that the time series are annual averages. The “monthly”  
 530 approach in Section 1.2.1 of the SI is the same as the seasonal approach in Equation d, except

531 instead of a four regressions, twelve are performed, with all time series being monthly averages  
 532 sampled every twelve months. The “all months” approach instead performs only one regression,  
 533 just like the annual approach, except that monthly average time series are used instead of annual  
 534 averages (the logic being that even though months may have different properties, there may be an  
 535 advantage in maximizing the data available to fit a regression).

536 *e. Estimating the forced response*

537 1) FORCED FEEDBACKS

538 Suppose that we have a  $n_{time,abrupt4x}$ -year long abrupt4x simulation of a GCM for which we  
 539 have spatial feedbacks estimated from a control run. We then define an early period (years 2 to 20)  
 540 and a late period (years 21 to  $n_{time,abrupt4x}$ ). The true feedbacks  $\lambda_{f,p}$  for the abrupt4x simulation  
 541 during each period  $p$  (where  $p$  is *early* or *late*) are defined as the slope of the least squares fit of  
 542 the linear regression of the time series of globally averaged TOA flux anomalies of type  $f$  from  
 543 the abrupt4x simulation ( $\vec{R}'_{f,abrupt4x}$ ), against the globally averaged surface temperature anomalies  
 544 from the abrupt4x simulation  $\vec{T}'_{abrupt4x}$ :

$$\lambda_{abrupt4x,f,p} = \frac{\{\vec{T}'_{abrupt4x}\}_p \cdot \{\vec{R}'_{f,abrupt4x}\}_p}{\|\{\vec{T}'_{abrupt4x}\}_p\|^2} \quad (\text{A4})$$

545 where the curly brackets denote that the time series are averaged over exponentially longer peri-  
 546 ods, with annual averages for the first decade increasing to centennial averages by the simulation’s  
 547 end, and the  $p$  subscript denotes whether values from before or after year 20 are used.  $\vec{R}'_{f,abrupt4x}$   
 548 and  $\vec{T}'_{abrupt4x}$  are vectors with as many entries as years in the abrupt4x simulation (1000 years).

549 We can make estimates of these feedbacks using the MR method by first estimating the abrupt4x  
 550 simulation’s TOA radiative flux of type  $f$  for each month of the year  $m$  by multiplying the surface

551 temperature time series of that abrupt4x simulation for that month,  $\mathbf{T}'_{m,abrupt4x}$  (a  $n_{time,abrupt4x} \times$   
 552  $n_{grid}$  matrix) by the spatial feedbacks for that month's season:

$$\hat{\mathbf{R}}'_{f,m,abrupt4x} = \mathbf{T}'_{m,abrupt4x} \Lambda_{f,s(m)} \quad (\text{A5})$$

553 We use months instead of seasonal averages because our seasons do not start in January, and  
 554 this approach allows us to have annual averages that start in January. These monthly time se-  
 555 ries  $\hat{\mathbf{R}}'_{f,m,abrupt4x}$  can then be turned into annual averages  $\hat{\mathbf{R}}'_{f,abrupt4x}$ , and then global averages  
 556  $\hat{\vec{R}}'_{f,abrupt4x}$ , allowing us to estimate the feedbacks for period  $p$  by performing the same least squares  
 557 fit as above:

$$\hat{\lambda}_{abrupt4x,f,p} = \frac{\{\vec{T}'_{abrupt4x,p}\} \cdot \{\hat{\vec{R}}'_{f,abrupt4x,p}\}}{\|\{\vec{T}'_{abrupt4x,p}\}\|^2} \quad (\text{A6})$$

## 558 2) SPATIAL PATTERNS OF TOA FLUX CHANGE

559 We quantify the normalized spatial pattern of TOA radiative flux change of flux type  $f$  across  
 560 a period  $p$  by taking a finite difference approach, taking the mean value of  $\vec{R}'_{f,abrupt4x}$  during two  
 561 parts of the period and subtracting the first part from the second (where the divisions for the *early*  
 562 period are years 2-6 and 7-20, and the divisions for the *late* period are 21-170 and 171- $n_{time,abrupt4x}$ ,  
 563 with both divisions chosen to allow for substantial warming in each period), and then dividing this  
 564 by the average change in the globally averaged surface temperature between these two periods:

$$\Delta \vec{R}'_{f,abrupt4x,p} = \frac{\left( \sum_{i=t_{mid,p}+1}^{t_{end,p}} \begin{bmatrix} R'_{f,abrupt4x,i,1} \\ R'_{f,abrupt4x,i,2} \\ \vdots \\ R'_{f,abrupt4x,n_{grid}} \end{bmatrix} - \sum_{i=t_{start,p}}^{t_{mid,p}} \begin{bmatrix} R'_{f,abrupt4x,i,1} \\ R'_{f,abrupt4x,i,2} \\ \vdots \\ R'_{f,abrupt4x,n_{grid}} \end{bmatrix} \right)}{\left( \sum_{i=t_{mid,p}+1}^{t_{end,p}} T_{abrupt4x,i} - \sum_{i=t_{start,p}}^{t_{mid,p}} T_{abrupt4x,i} \right)} \quad (\text{A7})$$

565 where  $t_{start,p}$  and  $t_{end,p}$  are the first and last years in period  $p$ , respectively, where  $t_{mid,p}$  is 6 for  
 566 the early period and 170 for late period, where  $R'_{f,abrupt4x,i,j}$  is the element in the  $i^{th}$  row and  $j^{th}$   
 567 column of  $\mathbf{R}'_{f,abrupt4x}$ , and where  $T_{abrupt4x,i}$  is the  $i^{th}$  element in  $\vec{T}_{abrupt4x}$ . Finite difference is used  
 568 instead of regressing values against a global average because the presence of local and nonlocal  
 569 feedbacks causes nonlinear relationships between  $N'_i(t)$  and  $T'_i(t)$  (or  $\vec{T}'(t)$ ), which would lead to  
 570 biased estimates of change from a linear regression.

571 *f. Errors*

572 We calculate two types of errors: feedback errors (Tables 1 and S2), and spatial errors (Tables 2  
 573 and S3). We add a subscript  $g$  to our feedbacks and spatial patterns of TOA flux change to signify  
 574 that they belong to the GCM  $g$ , where  $g$  is one of CCSM3, CESM104, GISSE2R, HadCM3L,  
 575 IPSLCM5A, and MPIESM12. The feedback error is given by the root mean square error:

$$\epsilon_{feedback,f,p} = \sqrt{\frac{1}{n_{GCMs}} \sum_{g \in GCMs} (\hat{\lambda}_{f,abrupt4x,p,g} - \lambda_{f,abrupt4x,p,g})^2} \quad (A8)$$

576 where  $n_{GCMs}$  is 6, the number of AOGCMs. The spatial error is measured by taking the area-  
 577 weighted root mean square error of the spatial estimate

$$\epsilon_{spatial,f,p} = \sqrt{\frac{\sum_{i=1}^{n_{grid}} (\hat{\Delta}\vec{R}'_{f,abrupt4x,p,i} - \vec{R}'_{f,abrupt4x,p,i})^2 a_i}{\sum_{i=1}^{n_{grid}} a_i}} \quad (A9)$$

578 where  $a_i$  is the area of the  $i^{th}$  grid cell. For the spatial errors in the main body of the paper, this is  
 579 taken on multi-model mean values of  $\hat{\Delta}\vec{R}'_{f,abrupt4x,p,i}$  and  $\vec{R}'_{f,abrupt4x,p,i}$ . For the same calculation  
 580 for individual models (Table S4 and Figures S6-S8 in the supplementary materials), values for  
 581 each model are used instead.

582 *g. Other methods to calculate feedbacks*

583 We consider two other methods for deriving spatial feedbacks, estimating abrupt4x feedbacks,  
584 and estimating spatial patterns of TOA flux change:

585 1) THE GLOBAL METHOD

586 The seasonal version of the “global” method used in the main body of the paper is estimated  
587 using the least squares fit on this regression:

$$\lambda_{global,f,s} = \frac{\vec{T}'_s \cdot \vec{R}'_{f,s}}{\|\vec{T}'_s\|^2} \quad (A10)$$

588 where  $\vec{T}'_s$  and  $\vec{R}'_{f,s}$  are globally and seasonally averaged time series of control simulation surface  
589 temperature and TOA flux  $f$  respectively, sampled every fourth seasonal value so that all elements  
590 of the time series are from season  $s$ . The four seasonal feedbacks are used to recreate estimates of  
591 the global averaged time series  $\vec{R}'_{f,abrupt4x}$ , which in turn is used, as above, to estimate abrupt4x  
592 feedbacks. Once more, different averaging of the control time series and groupings of regression  
593 equations can be used to make the annual, monthly, and all months versions of this method featured  
594 in Tables S3 and S4.

595 The normalized spatial pattern of TOA flux change can be found by first estimating the “local  
596 contribution” (Boer and Yu 2003a,b; Crook et al. 2011; Zelinka et al. 2012; Andrews et al. 2015),  
597 using Equation 1, but replacing the time series vector  $\vec{R}'_{f,s}$  with the spatial time series matrix  
598  $\mathbf{R}'_{f,s}$  from above, and replacing the single feedback  $\lambda_{global,f,s}$  with the spatial vector of feedbacks,  
599  $\vec{\lambda}_{global,f}$ .

600 2) THE LOCAL METHOD

601 The “local” method assumes the statistical model

$$R'_i(t) = \lambda_{local,i} T'_i(t) + \varepsilon(t) \text{ for each region } i \quad (A11)$$

602 Spatial feedbacks are estimated using least squares:

$$\vec{\lambda}_{local,f} = \begin{bmatrix} \lambda_{local,f,1} \\ \lambda_{local,f,2} \\ \vdots \\ \lambda_{local,f,n_{grid}} \end{bmatrix} = \begin{bmatrix} \frac{\vec{T}'_1 \cdot \vec{R}'_{f,1}}{\|\vec{T}'_1\|^2} \\ \frac{\vec{T}'_2 \cdot \vec{R}'_{f,2}}{\|\vec{T}'_2\|^2} \\ \vdots \\ \frac{\vec{T}'_{n_{grid}} \cdot \vec{R}'_{f,n_{grid}}}{\|\vec{T}'_{n_{grid}}\|^2} \end{bmatrix} \quad (A12)$$

603 where  $\vec{T}'_i$  and  $\vec{R}'_{f,i}$  are the  $i^{th}$  rows of  $\mathbf{T}'$  and  $\mathbf{R}'_f$  respectively. We can then generate estimates of  
 604  $\mathbf{R}'_{f,abrupt4x}$  as above. We apply these estimates to Equations A6 and A7 to estimate forced global  
 605 feedbacks and spatial patterns of TOA flux change.

606 *h. Local regression*

607 We use LOESS (LOcally Estimated Scatterplot Smoothing; Cleveland and Devlin 1988) to take  
 608 local regression of scatterplots of  $\bar{N}$  vs  $\bar{T}'$ . LOESS uses a weighted regression of a certain number  
 609 of nearest neighbors, in our case 30. Full details can be found in the code for this paper listed  
 610 above and in the LocallyWeightedRegression.jl Julia package (<https://github.com/juliohm/LocallyWeightedRegression.jl>).

612 **References**

- 613 Andrews, T., J. M. Gregory, and M. J. Webb, 2015: The Dependence of Radiative Forcing and  
 614 Feedback on Evolving Patterns of Surface Temperature Change in Climate Models. *Journal of  
 615 Climate*, **28** (4), 1630–1648.
- 616 Andrews, T., and M. J. Webb, 2017: The Dependence of Global Cloud and Lapse Rate Feedbacks  
 617 on the Spatial Structure of Tropical Pacific Warming. *Journal of Climate*, **31** (2), 641–654.

- 618 Andrews, T., and Coauthors, 2018: Accounting for Changing Temperature Patterns Increases  
619 Historical Estimates of Climate Sensitivity. *Geophysical Research Letters*, **45** (16), 8490–  
620 8499, doi:10.1029/2018GL078887, URL <https://agupubs.onlinelibrary.wiley.com/doi/abs/10.1029/2018GL078887>.
- 621
- 622 Armour, K. C., 2017: Energy budget constraints on climate sensitivity in light of inconstant cli-  
623 mate feedbacks. *Nature Climate Change*, **7** (5), 331.
- 624 Armour, K. C., C. M. Bitz, and G. H. Roe, 2012: Time-Varying Climate Sensitivity from Regional  
625 Feedbacks. *Journal of Climate*, **26** (13), 4518–4534.
- 626 Arrhenius, P. S., 1896: XXXI. On the influence of carbonic acid in the air upon the temperature  
627 of the ground. *The London, Edinburgh, and Dublin Philosophical Magazine and Journal of*  
628 *Science*, **41** (251), 237–276, doi:10.1080/14786449608620846.
- 629 Bloch-Johnson, J., R. T. Pierrehumbert, and D. S. Abbot, 2015: Feedback temperature dependence  
630 determines the risk of high warming. *Geophysical Research Letters*, **42** (12), 2015GL064240.
- 631 Boer, G., and B. Yu, 2003a: Climate sensitivity and response. *Climate Dynamics*, **20** (4), 415–429.
- 632 Boer, G. J., and B. Yu, 2003b: Climate sensitivity and climate state. *Climate Dynamics*, **21** (2),  
633 167–176.
- 634 Brown, P. T., W. Li, J. H. Jiang, and H. Su, 2015: Unforced Surface Air Temperature Variability  
635 and Its Contrasting Relationship with the Anomalous TOA Energy Flux at Local and Global  
636 Spatial Scales. *Journal of Climate*, **29** (3), 925–940.
- 637 Ceppi, P., and J. M. Gregory, 2017: Relationship of tropospheric stability to climate sensitivity and  
638 Earth’s observed radiation budget. *Proceedings of the National Academy of Sciences*, **114** (50),  
639 13 126–13 131.

- 640 Ceppi, P., and J. M. Gregory, 2019: A refined model for the Earths global energy balance. *Climate*  
641 *Dynamics*, **53** (7), 4781–4797, doi:10.1007/s00382-019-04825-x, URL <https://doi.org/10.1007/s00382-019-04825-x>.
- 642
- 643 Charney, J. G., and Coauthors, 1979: *Carbon Dioxide and Climate: A Scientific Assessment*. doi:  
644 10.17226/12181.
- 645 Choi, Y.-S., H. Cho, C.-H. Ho, R. S. Lindzen, S. K. Park, and X. Yu, 2014: Influence of  
646 non-feedback variations of radiation on the determination of climate feedback. *Theoretical*  
647 *and Applied Climatology*, **115** (1), 355–364, doi:10.1007/s00704-013-0998-6, URL <https://doi.org/10.1007/s00704-013-0998-6>.
- 648
- 649 Cleveland, W. S., and S. J. Devlin, 1988: Locally Weighted Regression: An Approach to Re-  
650 gression Analysis by Local Fitting. *Journal of the American Statistical Association*, **83** (403),  
651 596–610, doi:10.2307/2289282, URL <https://www.jstor.org/stable/2289282>.
- 652
- 653 Colman, R., and L. Hanson, 2017: On the relative strength of radiative feedbacks under climate  
variability and change. *Climate Dynamics*, **49** (5-6), 2115–2129.
- 654
- 655 Cox, P. M., C. Huntingford, and M. S. Williamson, 2018: Emergent constraint on equilibrium  
climate sensitivity from global temperature variability. *Nature*, **553** (7688), 319–322, doi:10.  
656 1038/nature25450, URL <https://www.nature.com/articles/nature25450>.
- 657
- 658 Crook, J. A., P. M. Forster, and N. Stuber, 2011: Spatial Patterns of Modeled Climate Feedback and  
Contributions to Temperature Response and Polar Amplification. *Journal of Climate*, **24** (14),  
659 3575–3592.
- 660
- 661 Dessler, A. E., 2010: A Determination of the Cloud Feedback from Climate Variations over the  
Past Decade. *Science*, **330** (6010), 1523–1527.

- 662 Dessler, A. E., 2012: Observations of Climate Feedbacks over 2000-10 and Comparisons to Cli-  
663 mate Models. *Journal of Climate*, **26** (1), 333–342.
- 664 Dessler, A. E., T. Mauritsen, and B. Stevens, 2018: The influence of internal variability on Earth's  
665 energy balance framework and implications for estimating climate sensitivity. *Atmospheric*  
666 *Chemistry and Physics*, **18** (7), 5147–5155, doi:<https://doi.org/10.5194/acp-18-5147-2018>,  
667 URL <https://www.atmos-chem-phys.net/18/5147/2018/>.
- 668 Dong, Y., C. Proistosescu, K. C. Armour, D. S. Battisti, Y. Dong, C. Proistosescu, K. C.  
669 Armour, and D. S. Battisti, 2019: Attributing Historical and Future Evolution of Radia-  
670 tive Feedbacks to Regional Warming Patterns using a Green's Function Approach: The Pre-  
671 eminance of the Western Pacific. *Journal of Climate*, doi:[10.1175/JCLI-D-18-0843.1](https://doi.org/10.1175/JCLI-D-18-0843.1), URL  
672 <https://journals.ametsoc.org/doi/abs/10.1175/JCLI-D-18-0843.1>.
- 673 Feldl, N., and G. H. Roe, 2013a: Four perspectives on climate feedbacks. *Geophysical Research*  
674 *Letters*, **40** (15), 4007–4011.
- 675 Feldl, N., and G. H. Roe, 2013b: The Nonlinear and Nonlocal Nature of Climate Feedbacks.  
676 *Journal of Climate*, **26** (21), 8289–8304, doi:[10.1175/JCLI-D-12-00631.1](https://doi.org/10.1175/JCLI-D-12-00631.1).
- 677 Forster, P. M. F., and J. M. Gregory, 2006: The Climate Sensitivity and Its Components Diagnosed  
678 from Earth Radiation Budget Data. *Journal of Climate*, **19** (1), 39–52.
- 679 Fueglistaler, S., 2019: Observational Evidence for Two Modes of Coupling Between Sea Surface  
680 Temperatures, Tropospheric Temperature Profile, and Shortwave Cloud Radiative Effect in the  
681 Tropics. *Geophysical Research Letters*, **46** (16), 9890–9898, doi:[10.1029/2019GL083990](https://doi.org/10.1029/2019GL083990), URL  
682 <https://agupubs.onlinelibrary.wiley.com/doi/abs/10.1029/2019GL083990>.

- 683 Gregory, J., and M. Webb, 2008: Tropospheric Adjustment Induces a Cloud Component in CO2  
684 Forcing. *Journal of Climate*, **21** (1), 58–71, doi:10.1175/2007JCLI1834.1.
- 685 Gregory, J. M., and T. Andrews, 2016: Variation in climate sensitivity and feedback  
686 parameters during the historical period. *Geophysical Research Letters*, **43** (8), 3911–  
687 3920, doi:10.1002/2016GL068406, URL <https://agupubs.onlinelibrary.wiley.com/doi/abs/10.1002/2016GL068406>.
- 688
- 689 Gregory, J. M., R. J. Stouffer, S. C. B. Raper, P. A. Stott, and N. A. Rayner, 2002: An Obser-  
690 vationally Based Estimate of the Climate Sensitivity. *Journal of Climate*, **15** (22), 3117–3121,  
691 doi:10.1175/1520-0442(2002)015<3117:AOBEOT>2.0.CO;2.
- 692 Jiménez-de-la Cuesta, D., and T. Mauritsen, 2019: Emergent constraints on Earths transient  
693 and equilibrium response to doubled CO 2 from post-1970s global warming. *Nature Geo-  
694 science*, **12** (11), 902–905, doi:10.1038/s41561-019-0463-y, URL <https://www.nature.com/articles/s41561-019-0463-y>.
- 695
- 696 Jonko, A. K., K. M. Shell, B. M. Sanderson, and G. Danabasoglu, 2012: Climate Feedbacks in  
697 CCSM3 under Changing CO2 Forcing. Part II: Variation of Climate Feedbacks and Sensitivity  
698 with Forcing. *Journal of Climate*, **26** (9), 2784–2795, doi:10.1175/JCLI-D-12-00479.1.
- 699
- 700 Klein, S. A., A. Hall, J. R. Norris, and R. Pincus, 2017: Low-Cloud Feedbacks from Cloud-  
701 Controlling Factors: A Review. *Surveys in Geophysics*, **38** (6), 1307–1329.
- 702
- 703 Klein, S. A., and D. L. Hartmann, 1993: The Seasonal Cycle of Low Stratiform Clouds. *Journal*  
704 *of Climate*, **6** (8), 1587–1606.
- 705
- 706 Klein, S. A., B. J. Soden, and N.-C. Lau, 1999: Remote Sea Surface Temperature Variations during  
707 ENSO: Evidence for a Tropical Atmospheric Bridge. *Journal of Climate*, **12** (4), 917–932, doi:

- 705 10.1175/1520-0442(1999)012<0917:RSSTVD>2.0.CO;2, URL <https://journals.ametsoc.org/doi/full/10.1175/1520-0442%281999%29012%3C0917%3ARSSTVD%3E2.0.CO%3B2>.
- 706
- 707 708 709 Koll, D. D. B., and T. W. Cronin, 2018: Earth's outgoing longwave radiation linear due to H<sub>2</sub>O greenhouse effect. *Proceedings of the National Academy of Sciences*, **115** (41), 10 293–10 298, doi:10.1073/pnas.1809868115, URL <https://www.pnas.org/content/115/41/10293>.
- 710 711 712 Leconte, J., F. Forget, B. Charnay, R. Wordsworth, and A. Pottier, 2013: Increased insolation threshold for runaway greenhouse processes on Earth-like planets. *Nature*, **504** (7479), 268–271, doi:10.1038/nature12827.
- 713 714 715 Lewis, N., and J. Curry, 2018: The Impact of Recent Forcing and Ocean Heat Uptake Data on Estimates of Climate Sensitivity. *Journal of Climate*, **31** (15), 6051–6071, doi:10.1175/JCLI-D-17-0667.1.
- 716 717 Lewis, N., and J. A. Curry, 2015: The implications for climate sensitivity of AR5 forcing and heat uptake estimates. *Climate Dynamics*, **45** (3-4), 1009–1023.
- 718 719 720 721 Li, W., and C. E. Forest, 2014: Estimating the Sensitivity of the Atmospheric Teleconnection Patterns to SST Anomalies Using a Linear Statistical Method. *Journal of Climate*, **27** (24), 9065–9081, doi:10.1175/JCLI-D-14-00231.1, URL <https://journals.ametsoc.org/doi/full/10.1175/JCLI-D-14-00231.1>.
- 722 723 724 725 Li, W., C. E. Forest, and J. Barsugli, 2012: Comparing two methods to estimate the sensitivity of regional climate simulations to tropical SST anomalies. *Journal of Geophysical Research: Atmospheres*, **117** (D20), doi:10.1029/2011JD017186, URL <https://agupubs.onlinelibrary.wiley.com/doi/abs/10.1029/2011JD017186>.

- 726 Libardoni, A. G., C. E. Forest, A. P. Sokolov, and E. Monier, 2019: Underestimating Internal Vari-  
727 ability Leads to Narrow Estimates of Climate System Properties. *Geophysical Research Letters*,  
728 **46** (16), 10 000–10 007, doi:10.1029/2019GL082442, URL <https://agupubs.onlinelibrary.wiley.com/doi/abs/10.1029/2019GL082442>.
- 730 Lindzen, R. S., M.-D. Chou, and A. Y. Hou, 2001: Does the Earth Have an Adaptive In-  
731frared Iris? *Bulletin of the American Meteorological Society*, **82** (3), 417–432, doi:10.1175/1520-0477(2001)082<0417:DTEHAA>2.3.CO;2, URL <https://journals.ametsoc.org/doi/abs/10.1175/1520-0477%282001%29082%3C0417%3ADTEHAA%3E2.3.CO%3B2>.
- 734 Liu, F., J. Lu, O. Garuba, L. R. Leung, Y. Luo, and X. Wan, 2018: Sensitivity of Surface  
735 Temperature to Oceanic Forcing via q-Flux Greens Function Experiments. Part I: Linear Re-  
736 sponse Function. *Journal of Climate*, **31** (9), 3625–3641, doi:10.1175/JCLI-D-17-0462.1, URL  
737 <https://journals.ametsoc.org/doi/10.1175/JCLI-D-17-0462.1>.
- 738 Liu, Z., N. Wen, and Y. Liu, 2008: On the Assessment of Nonlocal Climate Feedback. Part I:  
739 The Generalized Equilibrium Feedback Assessment. *Journal of Climate*, **21** (1), 134–148, doi:  
740 10.1175/2007JCLI1826.1, URL <http://journals.ametsoc.org/doi/abs/10.1175/2007JCLI1826.1>.
- 741 Lutsko, N. J., and M. Popp, 2019: Probing the Sources of Uncertainty in Transient  
742 Warming on Different Timescales. *Geophysical Research Letters*, **46** (20), 11 367–11 377,  
743 doi:10.1029/2019GL084018, URL <https://agupubs.onlinelibrary.wiley.com/doi/abs/10.1029/2019GL084018>.
- 745 Lutsko, N. J., and K. Takahashi, 2018: What Can the Internal Variability of CMIP5 Models Tell  
746 Us about Their Climate Sensitivity? *Journal of Climate*, **31** (13), 5051–5069, doi:10.1175/  
747 JCLI-D-17-0736.1.

- 748 Mauritsen, T., and B. Stevens, 2015: Missing iris effect as a possible cause of muted hydrological  
749 change and high climate sensitivity in models. *Nature Geoscience*, **8** (5), 346–351, doi:10.1038/  
750 ngeo2414, URL <https://www.nature.com/articles/ngeo2414>.
- 751 Meraner, K., T. Mauritsen, and A. Voigt, 2013: Robust increase in equilibrium climate sensitivity  
752 under global warming. *Geophysical Research Letters*, **40** (22), 5944–5948.
- 753 Murphy, D. M., S. Solomon, R. W. Portmann, K. H. Rosenlof, P. M. Forster, and T. Wong, 2009:  
754 An observationally based energy balance for the Earth since 1950. *Journal of Geophysical Re-*  
755 *search: Atmospheres*, **114** (D17).
- 756 Murphy, J. M., 1995: Transient Response of the Hadley Centre Coupled Ocean-Atmosphere  
757 Model to Increasing Carbon Dioxide. Part 1: Control Climate and Flux Adjustment. *Journal*  
758 *of Climate*, **8** (1), 36–56.
- 759 Otto, A., and Coauthors, 2013: Energy budget constraints on climate response. *Nature Geoscience*,  
760 **6** (6), 415.
- 761 Po-Chedley, S., K. C. Armour, C. M. Bitz, M. D. Zelinka, B. D. Santer, and Q. Fu, 2018: Sources  
762 of intermodel spread in the lapse rate and water vapor feedbacks. *Journal of Climate*.
- 763 Proistosescu, C., A. Donohoe, K. C. Armour, G. H. Roe, M. F. Stuecker, and C. M. Bitz, 2018: Ra-  
764 diative Feedbacks From Stochastic Variability in Surface Temperature and Radiative Imbalance.  
765 *Geophysical Research Letters*, **45** (10), 5082–5094, doi:10.1029/2018GL077678.
- 766 Proistosescu, C., and P. J. Huybers, 2017: Slow climate mode reconciles historical and model-  
767 based estimates of climate sensitivity. *Science Advances*, **3** (7), e1602 821, doi:10.1126/sciadv.  
768 1602821.

- 769 Roe, G. H., and M. B. Baker, 2007: Why Is Climate Sensitivity So Unpredictable? *Science*,  
770 **318 (5850)**, 629–632, doi:10.1126/science.1144735.
- 771 Rose, B. E. J., K. C. Armour, D. S. Battisti, N. Feldl, and D. D. B. Koll, 2014: The dependence of  
772 transient climate sensitivity and radiative feedbacks on the spatial pattern of ocean heat uptake.  
773 *Geophysical Research Letters*, **41 (3)**, 1071–1078.
- 774 Rose, B. E. J., and L. Rayborn, 2016: The Effects of Ocean Heat Uptake on Transient Climate  
775 Sensitivity. *Current Climate Change Reports*, **2 (4)**, 190–201.
- 776 Rugenstein, M., and Coauthors, 2019: LongRunMIP - motivation and design for a large col-  
777 lection of millennial-length AO-GCM simulations. *Bulletin of the American Meteorological  
778 Society*, doi:10.1175/BAMS-D-19-0068.1, URL [https://journals.ametsoc.org/doi/abs/10.1175/  
779 BAMS-D-19-0068.1](https://journals.ametsoc.org/doi/abs/10.1175/BAMS-D-19-0068.1).
- 780 Rugenstein, M. A. A., K. Caldeira, and R. Knutti, 2016: Dependence of global radiative feedbacks  
781 on evolving patterns of surface heat fluxes. *Geophysical Research Letters*, **43 (18)**, 9877–9885,  
782 doi:10.1002/2016GL070907.
- 783 Seager, R., M. Cane, N. Henderson, D.-E. Lee, R. Abernathey, and H. Zhang, 2019: Strengthening  
784 tropical Pacific zonal sea surface temperature gradient consistent with rising greenhouse gases.  
785 *Nature Climate Change*, **9 (7)**, 517–522, doi:10.1038/s41558-019-0505-x, URL <https://www.nature.com/articles/s41558-019-0505-x>.
- 786 Senior, C. A., and J. F. B. Mitchell, 2000: The time-dependence of climate sensitivity. *Geophysical  
787 Research Letters*, **27 (17)**, 2685–2688.
- 788 Soden, B. J., A. J. Broccoli, and R. S. Hemler, 2004: On the Use of Cloud Forcing to Estimate  
789 Cloud Feedback. *Journal of Climate*, **17 (19)**, 3661–3665.

- 791 Spencer, R. W., and W. D. Braswell, 2008: Potential Biases in Feedback Diagnosis from Observa-  
792 tional Data: A Simple Model Demonstration. *Journal of Climate*, **21** (21), 5624–5628, doi:10.  
793 1175/2008JCLI2253.1, URL <https://journals.ametsoc.org/doi/full/10.1175/2008JCLI2253.1>.
- 794 Spencer, R. W., and W. D. Braswell, 2011: On the Misdiagnosis of Surface Temperature Feed-  
795 backs from Variations in Earth’s Radiant Energy Balance. *Remote Sensing*, **3** (8), 1603–1613,  
796 doi:10.3390/rs3081603, URL <https://www.mdpi.com/2072-4292/3/8/1603>.
- 797 Trenberth, K. E., Y. Zhang, J. T. Fasullo, and S. Taguchi, 2015: Climate variability and relation-  
798 ships between top-of-atmosphere radiation and temperatures on Earth. *Journal of Geophysical*  
799 *Research: Atmospheres*, **120** (9), 3642–3659, doi:10.1002/2014JD022887.
- 800 Watterson, I. G., 2000: Interpretation of Simulated Global Warming Using a Simple Model. *Jour-  
801 nal of Climate*, **13** (1), 202–215.
- 802 Wetherald, R. T., and S. Manabe, 1988: Cloud Feedback Processes in a General Circulation  
803 Model. *Journal of the Atmospheric Sciences*, **45** (8), 1397–1416, doi:10.1175/1520-0469(1988)  
804 045⟨1397:CFPIAG⟩2.0.CO;2.
- 805 Winton, M., K. Takahashi, and I. M. Held, 2010: Importance of Ocean Heat Uptake Efficacy to  
806 Transient Climate Change. *Journal of Climate*, **23** (9), 2333–2344, doi:10.1175/2009JCLI3139.  
807 1.
- 808 Wood, R., and C. S. Bretherton, 2006: On the Relationship between Stratiform Low Cloud Cover  
809 and Lower-Tropospheric Stability. *Journal of Climate*, **19** (24), 6425–6432.
- 810 Zelinka, M. D., S. A. Klein, and D. L. Hartmann, 2012: Computing and Partitioning Cloud Feed-  
811 backs Using Cloud Property Histograms. Part I: Cloud Radiative Kernels. *Journal of Climate*,  
812 **25** (11), 3715–3735.

813 Zhou, C., M. D. Zelinka, and S. A. Klein, 2016: Impact of decadal cloud variations on the Earth's  
814 energy budget. *Nature Geoscience*, **9** (12), 871–874, doi:10.1038/ngeo2828, URL <https://www.nature.com/articles/ngeo2828>.

815  
816 Zhou, C., M. D. Zelinka, and S. A. Klein, 2017: Analyzing the dependence of global cloud feed-  
817 back on the spatial pattern of sea surface temperature change with a Green's function approach.  
818 *Journal of Advances in Modeling Earth Systems*, **9** (5), 2174–2189.

819 LIST OF TABLES

820	<b>Table 1.</b>	<i>Feedback errors.</i> Root mean square errors of estimates of abrupt4x feedbacks
821		( $\lambda_{4x,early}$ , $\lambda_{4x,late}$ ) and their change with time ( $\Delta\lambda_{4x}$ ), for net TOA fluxes and
822		each component flux (in $\text{Wm}^{-2}\text{K}^{-1}$ ) and for the seasonal versions of the three
823		methods presented in Section 2 (see Appendix for details). For annual and
824		monthly values, see Table S2, and for fluxes north of $30^\circ\text{S}$ , see Table S5. . . . .
		43
825	<b>Table 2.</b>	<i>Spatial errors.</i> The model-mean area-weighted root mean square error of esti-
826		mates of the warming-normalized change in TOA fluxes during the early and
827		late periods of the abrupt4x simulations, and the change in pattern between
828		these period (see Appendix for details). All values have units of $\text{Wm}^{-2}\text{K}^{-1}$ .
829		For annual and monthly versions in addition to seasonal, see Table S2, for in-
830		dividual models see Table S4, and for fluxes north of $30^\circ\text{S}$ , see Table S6. . . . .
		44

831 TABLE 1. *Feedback errors*. Root mean square errors of estimates of abrupt4x feedbacks ( $\lambda_{4x,early}$ ,  $\lambda_{4x,late}$ ) and  
 832 their change with time ( $\Delta\lambda_{4x}$ ), for net TOA fluxes and each component flux (in  $\text{Wm}^{-2}\text{K}^{-1}$ ) and for the seasonal  
 833 versions of the three methods presented in Section 2 (see Appendix for details). For annual and monthly values,  
 834 see Table S2, and for fluxes north of  $30^\circ\text{S}$ , see Table S5.

	net			LW clear			SW clear			LW cloud			SW cloud		
	MR	global	local	MR	global	local	MR	global	local	MR	global	local	MR	global	local
early	0.69	0.74	2.54	0.08	0.12	0.63	0.18	0.48	1.21	0.13	0.23	0.02	0.45	0.55	1.19
late	0.29	0.26	1.87	0.15	0.21	0.47	0.13	0.52	1.09	0.31	0.35	0.17	0.2	0.6	0.65
change	0.44	0.73	0.78	0.12	0.17	0.22	0.08	0.11	0.18	0.19	0.13	0.17	0.39	0.57	0.64

835 TABLE 2. *Spatial errors*. The model-mean area-weighted root mean square error of estimates of the warming-  
 836 normalized change in TOA fluxes during the early and late periods of the abrupt4x simulations, and the change  
 837 in pattern between these period (see Appendix for details). All values have units of  $\text{Wm}^{-2}\text{K}^{-1}$ . For annual and  
 838 monthly versions in addition to seasonal, see Table S2, for individual models see Table S4, and for fluxes north  
 839 of  $30^\circ\text{S}$ , see Table S6.

	<i>net</i>			<i>LW clear</i>			<i>SW clear</i>			<i>LW cloud</i>			<i>SW cloud</i>		
	MR	global	local	MR	global	local	MR	global	local	MR	global	local	MR	global	local
early	1.02	3.41	2.77	0.33	2.29	1.02	0.7	5.23	2.15	0.82	1.09	0.71	1.05	5.15	2.25
late	0.8	3.08	1.86	0.34	2.27	0.75	0.52	5.13	1.67	1.28	1.21	1.03	1.09	5.1	1.85
change	0.74	1.14	1.26	0.27	0.91	0.42	0.54	0.72	0.83	0.84	0.79	0.79	1.01	1.27	1.37

840 LIST OF FIGURES

**Fig. 1.** A schematic representation of the conceptual model used in Section 2, consisting of an overturning cell with a convecting (1) and a subsiding (2) region. Warming of the surface temperature  $T_1$  has nonlocal effects: it increases the horizontal heat transport  $H$ , and it changes properties of the atmosphere aloft in region 2 that affect its net top-of-atmosphere radiative flux,  $N_2$ , for instance by warming its free troposphere, increasing its lower tropospheric stability, and therefore increasing its low cloud cover. The dependence of  $N_2$  on  $T_1$  (holding  $T_2$  fixed) is an example of a nonlocal radiative feedback.

47

**Fig. 2.** Two experiments are performed with the conceptual model in Equation 1: an unforced “control” simulation (panels a,b) and a forced “abrupt4x” simulation (panels c,d). Values of  $\bar{N}$  vs.  $\bar{T}'$  from each experiment are given by the black dots in panels a and c, representing annual averages for the control simulation and exponentially increasing averages for the abrupt4x simulation. The global method assumes that the slope of the regression in panel a (blue line) gives the slope of the black dots in the lower left panel, underestimating the increase in this slope over time (blue lines and markers, panels c,d). The local method regresses  $N'_i$  against  $T'_i$  to estimate  $\lambda_i$  for both regions (dotted lines, panel b), which leads to an overestimate of the combined feedback associated with region 1 ( $\lambda_1 = \lambda_{1,1} + \lambda_{2,1}$ , dotted red line in panel b), and therefore an overestimate of the feedback early on (orange lines and markers, panels c,d). The MR method, given sufficient years to regress over, correctly estimates all spatial feedbacks (dashed lines, panel b), accurately predicting the feedbacks and its change with time (green lines and markers, panels c,d).

48

**Fig. 3.** Plots of  $\bar{N}$  vs.  $\bar{T}'$  for control simulations of six coupled atmosphere-ocean general circulation models (see Table S1 for details). We use the simulations to estimate spatial feedbacks using the global, local, and MR methods. We regrid simulations to  $15^\circ \times 15^\circ$  grids, giving 288 regions.

49

**Fig. 4.**  $\bar{N}$  vs.  $\bar{T}'$  for abrupt4x simulations of the same six GCMs from Figure 3 (black dots). Colored dots show estimates of  $\bar{N}_{\text{abrupt4x}}(t)$  made using the spatial feedbacks inferred from each model's control simulation and its spatial pattern of warming ( $\bar{T}'_{\text{abrupt4x}}(t)$ ) using the three methods described in the text; year one is not included in any method. Larger dots represent averages taken over exponentially increasing periods, except gray dots, which show all years. Solid lines show local regressions using LOESS. Global estimates for GISSE2R does not appear because it is nearly identical with MR estimates.

50

**Fig. 5.** True and estimated abrupt4x feedbacks as a function of time calculated using slopes of the local regression from Figure 4 (solid lines). Vertical dotted lines show the division between the early (2-20 years) and late (21-end) periods. Dots show true and estimated values of  $\lambda_{4x,early}$  and  $\lambda_{4x,later}$ . Feedbacks get more positive over time for all models. The MR and global methods initially overestimate feedbacks. The MR estimate increases with time as well, while the global method predicts a roughly constant feedback. The local method greatly overestimates the true feedback for all models except GISS-E2R. Figures S2-5 give the same plot for component fluxes.

51

**Fig. 6.** True vs. estimated feedbacks for the early (panels a, b, and c) and late (panels d, e, and f) periods and the change between them (panels g, h, and i). Black dots give values for the net feedback, while colored markers give values of the component feedbacks, which sum to the net feedback. The MR and global methods overestimate the early feedback due to SW cloud (red) feedbacks. The MR estimate of the late period has a small error across all components (panel d), while the global estimate has a smaller net error due to offsetting errors between LW and SW cloud feedbacks (panel e). As in Figure 5, the MR method is able to capture

some of the change in feedback, while the global method does not. The local method greatly overestimates the net feedback, primarily due to cloud feedbacks. Numerical values of the feedbacks are given in Table S7 and S8.

52

**Fig. 7.** Multi-model mean spatial pattern of net TOA flux change associated with the early (top row) and late (middle row) periods and the change between them (bottom row), calculated by taking the finite difference across each period. Changes are normalized by the total warming in each period, giving units of  $\text{Wm}^{-2}\text{K}^{-1}$ . The MR method is close to the true pattern except for overestimates south of  $30^\circ\text{S}$  and during the early period in the North Atlantic. This holds for individual flux components as well (Figures S9-S17). The global and local methods both have substantial errors over most of the globe. Figures S6-S8 show errors (estimates - true values) for the multi-model mean and individual models. . . . .

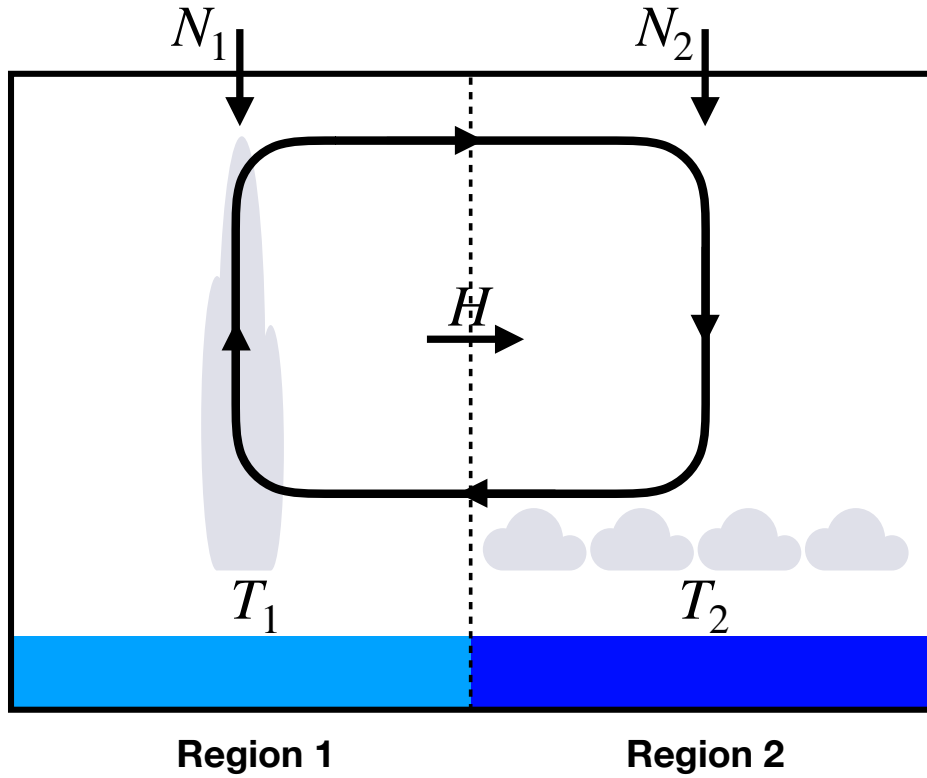
53

54

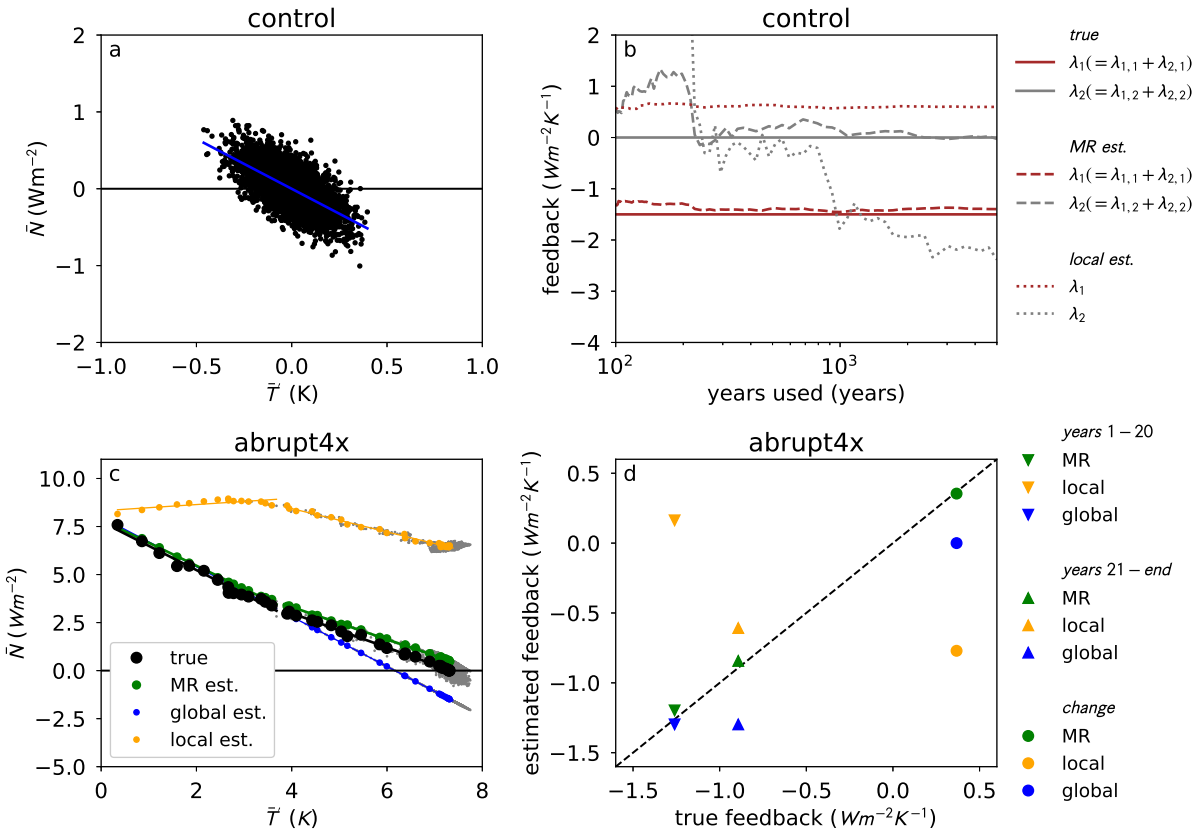
55

**Fig. 10.** Panel a shows the multi-model mean change in the pattern of warming between the abrupt4x early and late period, showing a shift towards regions of deep ocean heat uptake. Multiplying this pattern by MR-estimated spatial feedbacks gives an estimate of each grid cell's contribution to the change in feedback with time,  $\Delta\lambda_{4x}$  (panels b-f). Although the resulting patterns are patchy, there are positive contributions from tropical convecting regions via the SW cloud and LW clear feedbacks, and from regions of Southern Ocean sea ice in the SW clear feedback, as shown by the accompanying zonal averages. The LW clear feedback has a compensating negative term from the Southern Ocean, so that its total estimated contribution to  $\Delta\lambda_{4x}$  is smaller than the SW cloud feedback's (e.g., Figure S2 vs. Figure S5). . . .

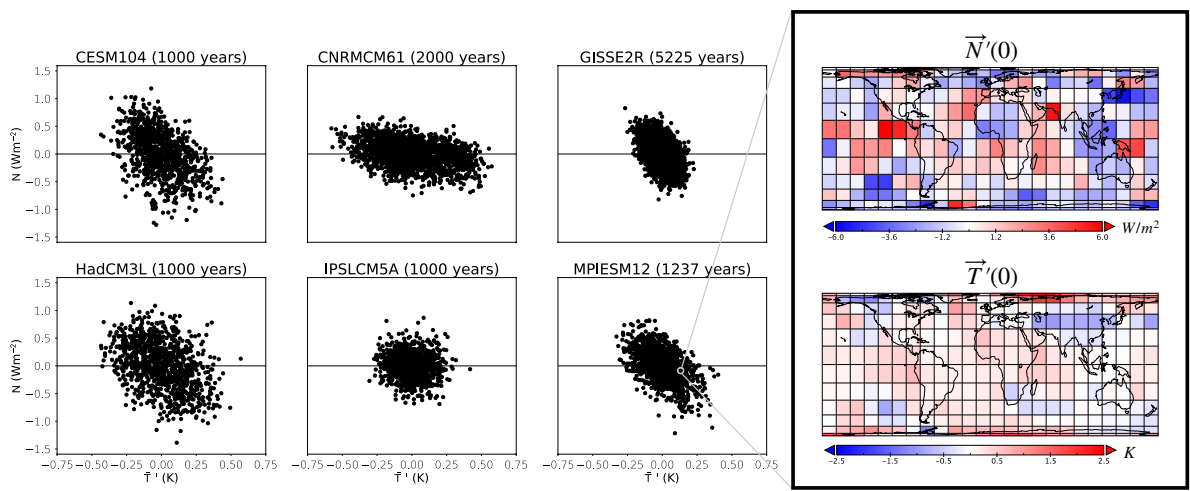
56



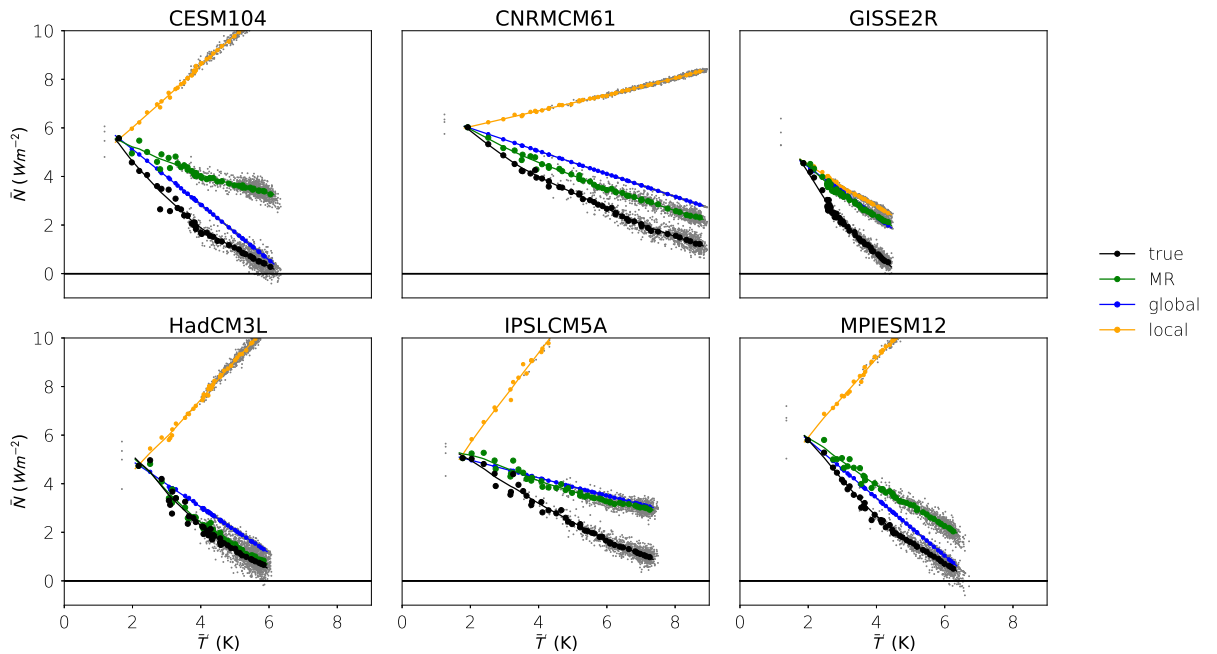
925 FIG. 1. A schematic representation of the conceptual model used in Section 2, consisting of an overturning  
 926 cell with a convecting (1) and a subsiding (2) region. Warming of the surface temperature  $T_1$  has nonlocal effects:  
 927 it increases the horizontal heat transport  $H$ , and it changes properties of the atmosphere aloft in region 2 that  
 928 affect its net top-of-atmosphere radiative flux,  $N_2$ , for instance by warming its free troposphere, increasing its  
 929 lower tropospheric stability, and therefore increasing its low cloud cover. The dependence of  $N_2$  on  $T_1$  (holding  
 930  $T_2$  fixed) is an example of a nonlocal radiative feedback.



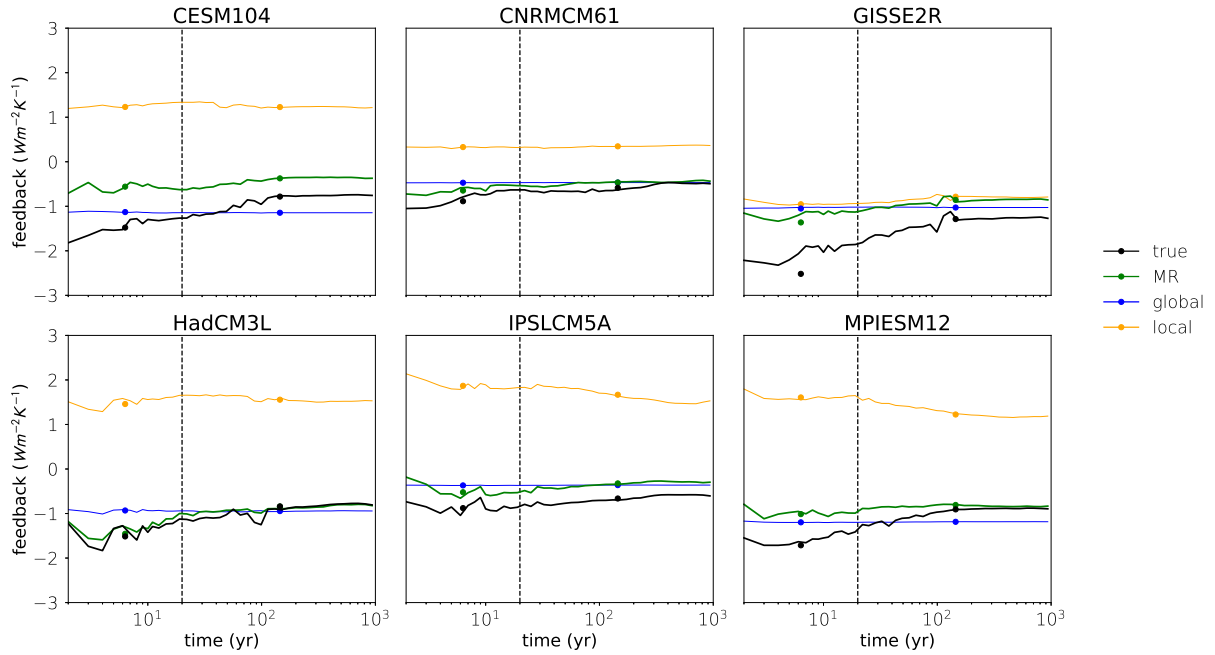
931 FIG. 2. Two experiments are performed with the conceptual model in Equation 1: an unforced “control”  
932 simulation (panels a,b) and a forced “abrupt4x” simulation (panels c,d). Values of  $\bar{N}$  vs.  $\bar{T}'$  from each experiment  
933 are given by the black dots in panels a and c, representing annual averages for the control simulation and  
934 exponentially increasing averages for the abrupt4x simulation. The global method assumes that the slope of  
935 the regression in panel a (blue line) gives the slope of the black dots in the lower left panel, underestimating the  
936 increase in this slope over time (blue lines and markers, panels c,d). The local method regresses  $N'_i$  against  $T'_i$   
937 to estimate  $\lambda_i$  for both regions (dotted lines, panel b), which leads to an overestimate of the combined feedback  
938 associated with region 1 ( $\lambda_1 = \lambda_{1,1} + \lambda_{2,1}$ , dotted red line in panel b), and therefore an overestimate of the  
939 feedback early on (orange lines and markers, panels c,d). The MR method, given sufficient years to regress  
940 over, correctly estimates all spatial feedbacks (dashed lines, panel b), accurately predicting the feedbacks and its  
941 change with time (green lines and markers, panels c,d).



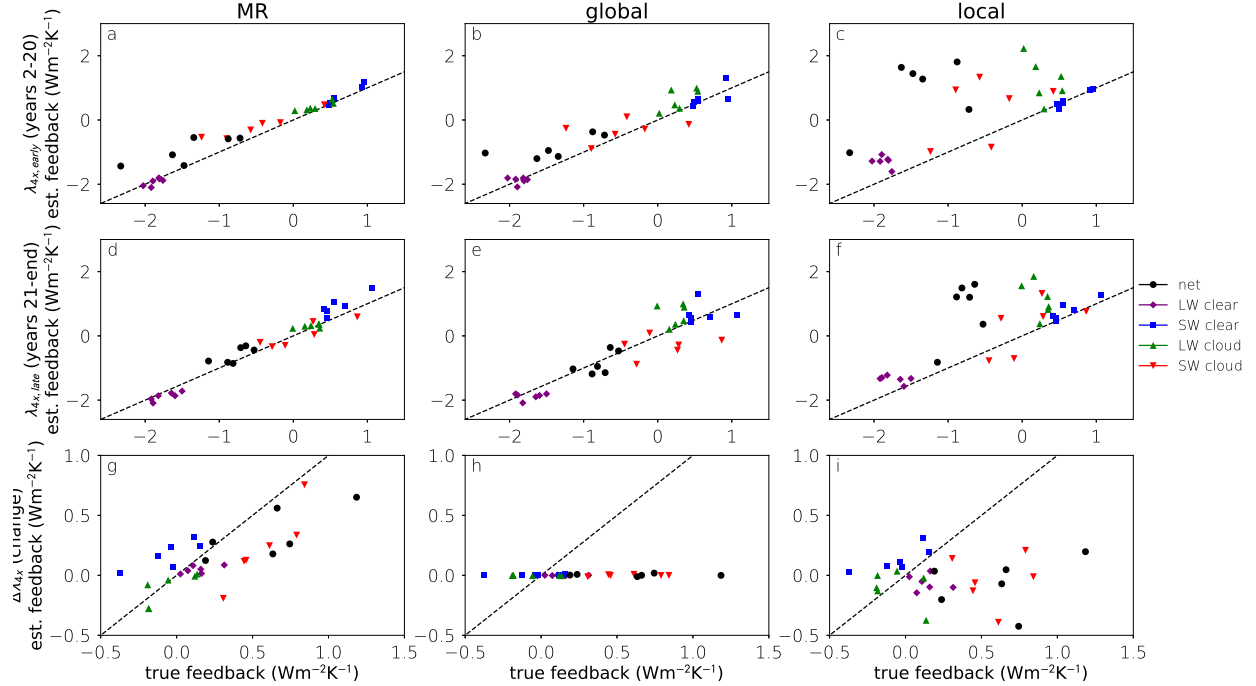
942 FIG. 3. Plots of  $\bar{N}$  vs.  $\bar{T}'$  for control simulations of six coupled atmosphere-ocean general circulation models  
 943 (see Table S1 for details). We use the simulations to estimate spatial feedbacks using the global, local, and MR  
 944 methods. We regrid simulations to  $15^\circ \times 15^\circ$  grids, giving 288 regions.



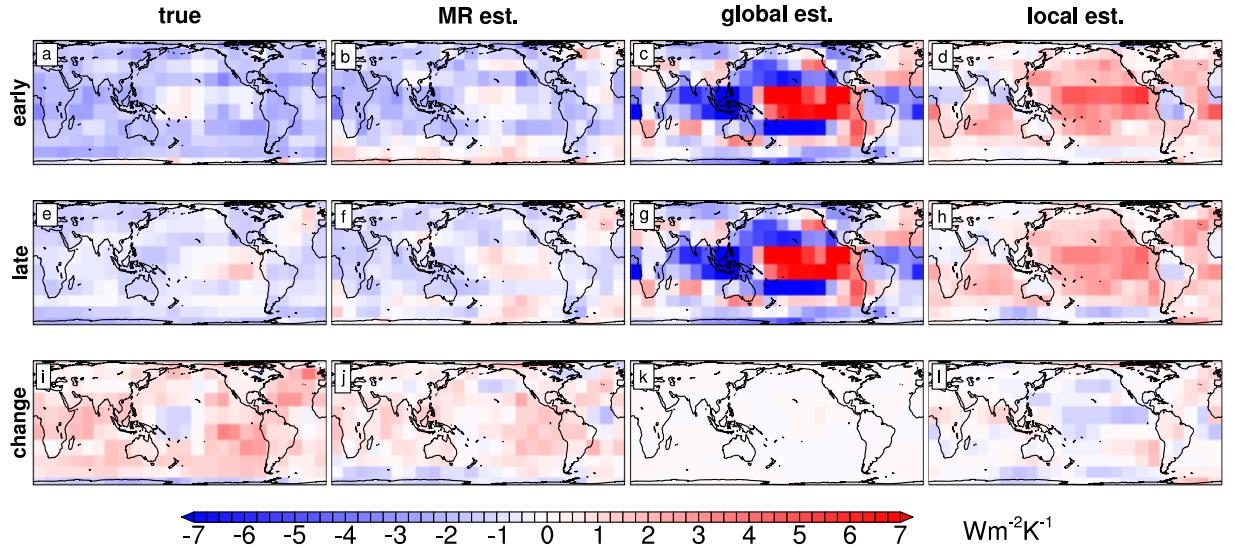
945 FIG. 4.  $\bar{N}$  vs.  $\bar{T}'$  for abrupt4x simulations of the same six GCMs from Figure 3 (black dots). Colored dots  
 946 show estimates of  $\bar{N}_{\text{abrupt4x}}(t)$  made using the spatial feedbacks inferred from each model's control simulation  
 947 and its spatial pattern of warming ( $\bar{T}'_{\text{abrupt4x}}(t)$ ) using the three methods described in the text; year one is not  
 948 included in any method. Larger dots represent averages taken over exponentially increasing periods, except gray  
 949 dots, which show all years. Solid lines show local regressions using LOESS. Global estimates for GISS-E2R  
 950 does not appear because it is nearly identical with MR estimates.



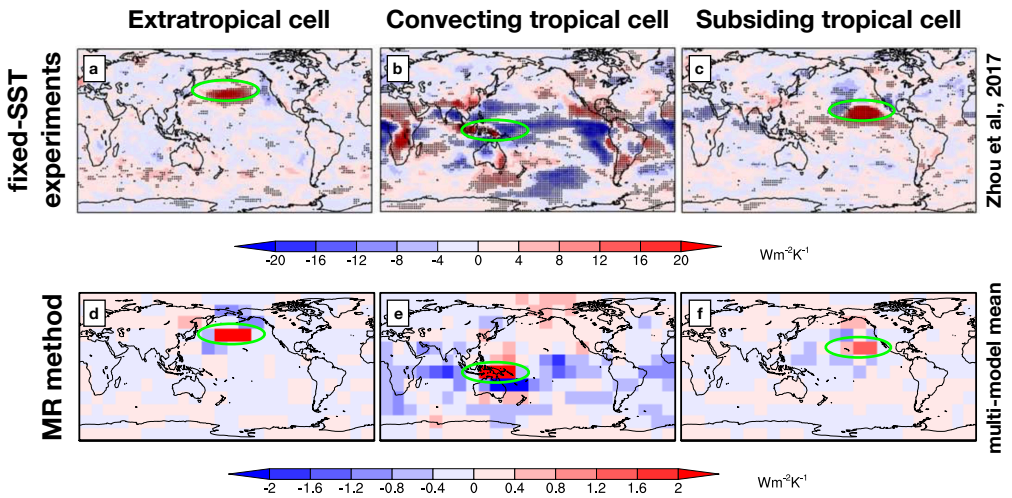
951 FIG. 5. True and estimated abrupt4x feedbacks as a function of time calculated using slopes of the local  
 952 regression from Figure 4 (solid lines). Vertical dotted lines show the division between the early (2-20 years) and  
 953 late (21-end) periods. Dots show true and estimated values of  $\lambda_{4x,early}$  and  $\lambda_{4x,later}$ . Feedbacks get more positive  
 954 over time for all models. The MR and global methods initially overestimate feedbacks. The MR estimate  
 955 increases with time as well, while the global method predicts a roughly constant feedback. The local method  
 956 greatly overestimates the true feedback for all models except GISS2R. Figures S2-5 give the same plot for  
 957 component fluxes.



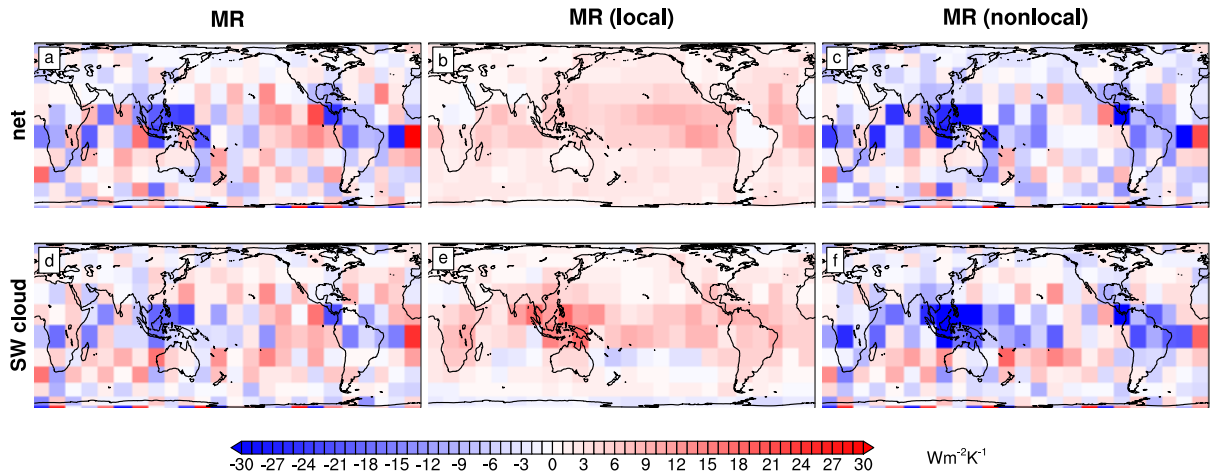
958 FIG. 6. True vs. estimated feedbacks for the early (panels a, b, and c) and late (panels d, e, and f) periods  
959 and the change between them (panels g, h, and i). Black dots give values for the net feedback, while colored  
960 markers give values of the component feedbacks, which sum to the net feedback. The MR and global methods  
961 overestimate the early feedback due to SW cloud (red) feedbacks. The MR estimate of the late period has a  
962 small error across all components (panel d), while the global estimate has a smaller net error due to offsetting  
963 errors between LW and SW cloud feedbacks (panel e). As in Figure 5, the MR method is able to capture some  
964 of the change in feedback, while the global method does not. The local method greatly overestimates the net  
965 feedback, primarily due to cloud feedbacks. Numerical values of the feedbacks are given in Table S7 and S8.



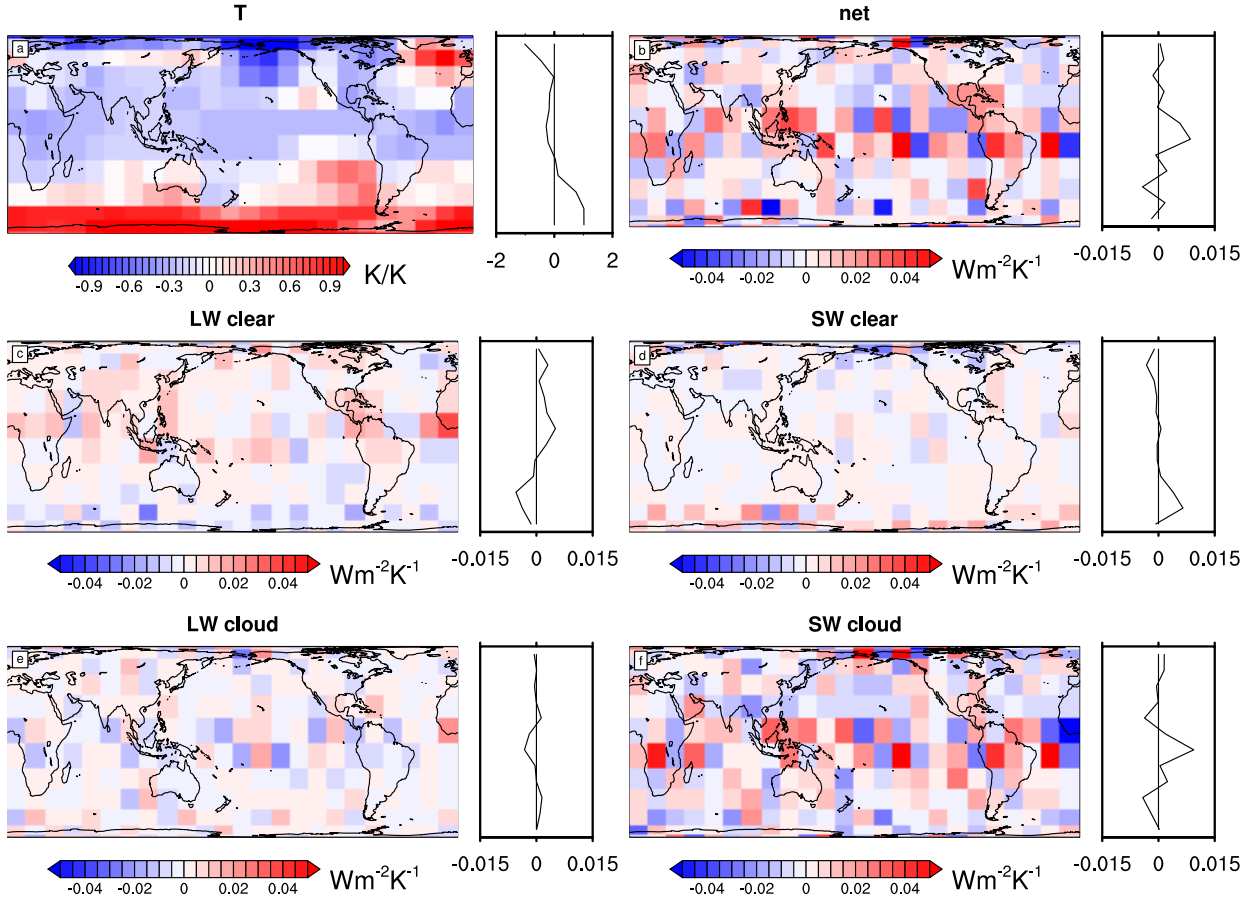
966 FIG. 7. Multi-model mean spatial pattern of net TOA flux change associated with the early (top row) and  
 967 late (middle row) periods and the change between them (bottom row), calculated by taking the finite difference  
 968 across each period. Changes are normalized by the total warming in each period, giving units of  $\text{Wm}^{-2}\text{K}^{-1}$ .  
 969 The MR method is close to the true pattern except for overestimates south of  $30^\circ\text{S}$  and during the early period  
 970 in the North Atlantic. This holds for individual flux components as well (Figures S9-S17). The global and local  
 971 methods both have substantial errors over most of the globe. Figures S6-S8 show errors (estimates - true values)  
 972 for the multi-model mean and individual models.



973 FIG. 8. Net cloud feedbacks associated with warming in regions circled in green estimated for CAM5 by  
 974 Zhou et al. (2017) using fixed-SST experiments (panels a, b, and c) or as a multi-model and multi-season mean  
 975 using the MR method (panels d, e, and f). For perturbations outside of tropical convecting regions (panels a,  
 976 c, d, and f), the effects are mostly local and positive, while perturbations in tropical convecting regions have  
 977 significant negative nonlocal effects in many regions of the Earth (panels b, e). Note that fixed-SST experiments  
 978 allow some land warming in response to these perturbations (panel b), while the MR method is agnostic about  
 979 whether the surface is land or ocean, and so does not include resulting land warming (panel e).



980 FIG. 9. Multi-model and multi-season mean spatial feedbacks estimated by the MR method. Panel a shows  
 981 the estimated change in  $\bar{N}$  caused by warming a degree in each cell as weighted by the cell's area. This is the  
 982 sum of local changes in  $\vec{N}$  (panel b), which are almost uniformly positive, and nonlocal changes (panel c), which  
 983 are usually negative, especially in regions of tropical convection. The competing positive local and negative  
 984 nonlocal components are primarily due to the SW cloud feedback (panels d, e, and f). For maps of all flux  
 985 components and assessments of uncertainty, see Figures S18-S22. For spatial feedbacks of all methods, see  
 986 Figure S23. Compare with estimates of spatial feedbacks for CAM4 in Figure 5c of Dong et al. (2019).



987 FIG. 10. Panel a shows the multi-model mean change in the pattern of warming between the abrupt4x early  
 988 and late period, showing a shift towards regions of deep ocean heat uptake. Multiplying this pattern by MR-  
 989 estimated spatial feedbacks gives an estimate of each grid cell's contribution to the change in feedback with  
 990 time,  $\Delta\lambda_{4x}$  (panels b-f). Although the resulting patterns are patchy, there are positive contributions from tropical  
 991 convecting regions via the SW cloud and LW clear feedbacks, and from regions of Southern Ocean sea ice in the  
 992 SW clear feedback, as shown by the accompanying zonal averages. The LW clear feedback has a compensating  
 993 negative term from the Southern Ocean, so that its total estimated contribution to  $\Delta\lambda_{4x}$  is smaller than the SW  
 994 cloud feedback's (e.g., Figure S2 vs. Figure S5).